An expansion–coalescence model to track gas bubble populations in magmas

Simona Mancini [a], Louis Forestier-Coste [b], Alain Burgisser [c,d,*], François James [a], Jonathan Castro [e]

[a] MAPMO, Université d'Orléans, Orléans, France
[b] IGPM, RWTH Aachen University, Aachen, Germany
[c] CNRS, ISTerre, F-73376 Le Bourget du Lac, France
[d] Université Savoie Mont Blanc, ISTerre, F-73376 Le Bourget du Lac, France
[e] Institute of Geosciences, Johannes Gutenberg University Mainz, Mainz, Germany

A R T I C L E   I N F O

A B S T R A C T

We propose a kinetic model that statistically describes the growth by decompression, exsolution and coalescence of a polydisperse population of gas bubbles in a silicate melt. The model is homogeneous in space and its main variable is a distribution function representing the probability to find a bubble of volume v and mass m at time t. The volume and mass growth rates are described by a simplification of the classical monodisperse bubble growth model. This simplification, which shortens computational time, removes the coupling between mass evolution and an advection–diffusion equation describing the behavior of the volatile concentration in the melt. We formulate three coalescence mechanisms: thinning of the inter-bubble planar films, film deformation by differential bubble pressure, and buoyancy-driven collision. Numerical simulations based on a semi-implicit numerical scheme show a good agreement between the coalescence-free runs and the monodisperse runs. When coalescence is introduced, numerical results show that coalescence kernels based on different physical mechanisms yield distinct evolutions of the size distributions. A preliminary comparison between runs and experimental data suggests a qualitative match of two out of the three proposed kernels. This kinetic model is thus a powerful tool that can help in assessing how bubble growth and coalescence occur in magmas.

© 2016 Elsevier B.V. All rights reserved.

1. Introduction

The remarkable link between the microphysics ruling gas bubbles that develop in magmas when they ascend in volcanic conduits and the large-scale dynamics of the resulting eruption is now firmly established. Bubble growth in viscous magmas is governed by decompression and exsolution of volatiles (mainly water) from the silicate melt into the bubbles themselves. This phenomena was first modeled by considering that the bubbles contained in a small volume of ascending magma are monodisperse, i.e. they all evolve in the same way and have the same radius, volume, mass, and pressure (Sparks, 1978). The most common model used since consists of a system of two ordinary differential equations describing the time evolution of the radius and mass of a single bubble that is coupled with an advection–diffusion equation modeling the space–time evolution of the volatile concentration in the melt surrounding the bubble (e.g., Toramaru, 1989, 1995; Proussevitch et al., 1993a; Proussevitch and Sahagian, 1998; Lyakhovsky et al., 1996; Navon et al., 1998; Lensky et al., 2001, 2004;

Nishimura, 2004; Chouet et al., 2006; Ichihara, 2008; Forestier-Coste et al., 2012; Chernov et al., 2014).

Although this monodisperse bubble population model predicts porosities and bubble sizes that match well with experimental data (e.g., Lyakhovsky et al., 1996; Forestier-Coste et al., 2012), it assumes that bubbles are isolated and therefore does not take into account their interactions, such as the coalescence of two (or more) bubbles. The polydisperse nature of a bubble population causes differential growth (e.g., Larsen and Gardner, 2000; Gardner, 2009), which can enhance coalescence (Castro et al., 2012). Neglecting coalescence is a severe limitation because of its large impact on the bubble size distribution (e.g., Larsen et al., 2004; Burgisser and Gardner, 2005; Iacono Marziano et al., 2007; Martel and Iacono-Marziano, 2015) and because coalescence can create an interconnected network of bubbles from which the gas can escape (e.g., Saar and Manga, 1999; Burgisser and Gardner, 2005; Takeuchi et al., 2005; Gardner, 2007; Rust and Cashman, 2011; Bai et al., 2010). Gas escape from magma is arguably the most important consequence of bubble coalescence because it has long been recognized as a main control of the transition between effusive and explosive eruptions (e.g., Eichelberger et al., 1986; Jaupart and Allègre, 1991; Woods and Koyaguchi, 1994; Degruyter et al., 2012).

There have been efforts to overcome the monodisperse assumption in models. A first category of studies comprises phenomenological

models that were aimed at reproducing natural size distributions (e.g., Blower, 2001; Blower et al., 2001; Gaonac'h et al., 1996, 2003, 2007). Very few studies populate the second category, which is composed of physical models (Lovejoy et al., 2004; L'Heureux, 2007). These physical models present a significant increment in complexity compared to monodisperse models. The model of L'Heureux (2007) considers the nucleation and growth of a polydisperse population of randomly located bubbles. The kinetic model of Lovejoy et al. (2004) describes the evolution of the distribution function of a set of bubbles that grow by decompression and coalescence. The distribution function represents the probability to find a bubble of a given volume at a specific time. The model is homogeneous in space. The volume growth rate is broadly defined as time dependent, and bubble coalescence is described by a Smoluchowski-type operator. Although it does not contain a numerical resolution of the full equation set, this work poses solid theoretical foundations to develop the next generation of model by providing solutions of simplified cases.

We propose a general kinetic model describing the evolution of a bubble population with vanishing velocities relative to the surrounding melt (i.e. valid in small magma volume where the population can be treated in a Lagrangian way). It is an extension of the kinetic model of Lovejoy et al. (2004) that includes growth mechanisms from the monodisperse model of Lensky et al. (2004) as formalized by Forestier-Coste et al. (2012) and coalescence mechanisms from Castro et al. (2012) and Lovejoy et al. (2004). The Methods and initial model section summarizes the monodisperse model that gives volume and mass evolution of each bubble class. The first section of the Results offers a simplification of this monodisperse model that avoids the coupling with the advection–diffusion equation and diminishes computational costs. A numerical study quantifies the error introduced by this simplification and the reader is referred to the Supplementary data to find B-growth, an open-source implementation of the monodisperse bubble growth model. We then propose suitable formulations of three coalescence operators. Since they depend on both the volume and the mass of the bubbles, these operators are best expressed in a two-dimensional form. Due to their complexity, two-dimensional coalescence operators have rarely been studied (Qamar and Warnecke, 2007a; Kumar et al., 2011). The abstract writing of the kinetic model follows in a rather classical way by means of Liouville's theorem and is in some sense a direct generalization of the Lovejoy et al. (2004) model. A summary of the discretization scheme is in Appendix A, and we use the numerical scheme developed in Forestier-Coste and Mancini (2012) for the coalescence kernel. Finally, we illustrate model capabilities by using a set of experimental data from Burgisser and Gardner (2005) and Castro et al. (2012).

2. Methods and initial model

2.1. Bubble size distributions of experimental samples

Numerical results are compared to four experimental samples described in Burgisser and Gardner (2005). The 2D analysis on thin sections reported in Burgisser and Gardner (2005) yielded a very small (~10) number of bubbles due to the restricted size of the 2D sections. Castro et al. (2012) re-analyzed some of these samples by Computed Tomography to increase the number of measured bubbles and improve the size distributions. We used the 3D reconstructed volume of sample PPE4 as described in Castro et al. (2012) and scanned samples PPE7, PPE10, and PPE11 using the same methodology so as to obtain 3D volumes of the samples with bubbles and melt separated in a binary fashion. De-coalescing was done by successively eroding the bubble network of one voxel-thick layer at a time with the ImageJ software (v. 1.47). De-coalesced bubble sizes were obtained by using the "Particle Analyzer" plugin of the BoneJ (version 1.3.11) bundle (Doube et al., 2010), from which equivalent diameters corrected for erosion numbers were calculated. The correction method used the measured surface area of each bubble multiplied by the number of erosions (generally 3). The

size distribution of PPE4 obtained using this method was very similar to that obtained by manually separating bubbles with the Blob3D software (Castro et al., 2012).

2.2. Monodisperse population modeling

In a viscous, crystal-free magma, the growth of a pre-existing monodisperse population of bubbles, i.e. of a set of bubbles of identical size at any given time and not interacting, can be described by giving the time, t, evolution of the radius, R, and mass, M, of one single bubble and assuming that it is surrounded by a spherical influence domain (i.e. the region of melt exchanging water with the bubble) of radius S (Proussevitch et al., 1993a; Fig. 1). Variables are summarized in Table 1. Subscripts 0 indicate initial values, diacritic dot indicates time differentiation. Diacritic tilde marks dimensional variables while its absence indicates dimensionless variables (hence t, R, M, and S are dimensionless). All the equations listed in the main text are given in dimensionless form, and Table S1 in the Supplementary data lists their dimensional counterparts. We use the mathematical formulation by Forestier-Coste et al. (2012) of the physical model proposed by Lensky et al. (2004). Briefly, these works describe the evolution of bubble radius and mass as a function of decompression and exsolution by the following dimensionless system of ordinary differential equations:

$$\dot{R} = \frac{R}{\eta \Theta_V} \left(P - P_a - \frac{\Sigma}{R} \right) \tag{1}$$
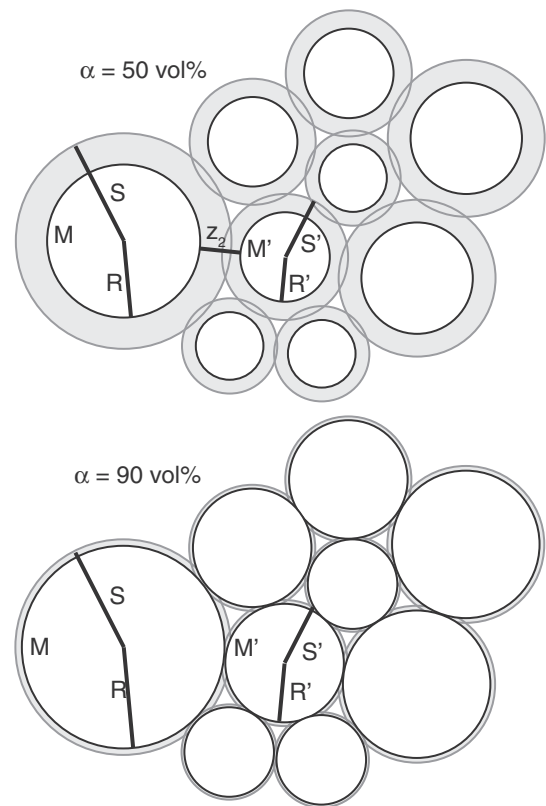

Fig. 1. Schematics of polydisperse arrangements of gas bubbles of radius R and mass M (white) with their surrounding melt shell of radius S (gray) that slightly overlap. Primes indicate the second bubble in a bubble pair considered by coalescence mechanisms, and z_1 is the distance between two bubbles in a pair. A) 50 vol.% porosity (α). B) 90 vol.% porosity (α). Drawings are scaled so as to represent 2D illustrations, albeit the models consider 3D spherical bubbles. Porosity is thus equal to R^2/S^2 (R^3/S^3 in 3D) and B) represents the maximum packing situation occurring at ~90 vol.% (60–70 vol.% in 3D, see Appendix B).

Table 1

Variable list. Symbols in parenthesis are initial values.

Dimensionless symbol	Dimensional symbol	Conversion	Variable
$a\ (a_0)$	$\tilde{a}\ (\tilde{a}_0)^{[a]}$	$\tilde{a} = a\tilde{R}_0$	Interbubble film radius (m)
A			Scaling constant
c	$\tilde{c}^{[a]}$	$\tilde{c} = c\tilde{R}_0\Delta\tilde{P}/\tilde{P}_0$	Average bubble growth rate (m/s)
$C\ (C_0)$			Melt water concentration
C_H	$\tilde{K}_H$	$C_H = \tilde{K}_H\sqrt{\tilde{P}_0}$	Solubility constant (Pa$^{-1/2}$)
C_T			Total water concentration (weight fraction)
D	$\tilde{D}\ (\tilde{D}_0)$	$\tilde{D} = D\tilde{D}_0$	Water diffusivity in melt (m^2/s)
$\mathcal{D}$			Discrete, non-normalized, volume and mass distribution
f	$\tilde{f}$	$f = \tilde{f}\tilde{V}_0\tilde{M}_0$	Size and mass distribution of bubbles (kg^{-1} m^{-3})
F	$\tilde{F}^{[a]}$	$F = F\tilde{R}_0\tilde{D}_0$	Water flux at bubble boundary (m^3/s)
H	$\tilde{H}^{[a]}$	$\tilde{H} = H\Delta\tilde{P}/\tilde{P}_0$	Coalescence kernel (1/s)
H_c	$\tilde{H}_c^{[a]}$	$\tilde{H}_c = H_c\Delta\tilde{P}/\tilde{P}_0$	Collision coalescence kernel (1/s)
H_f	$\tilde{H}_f^{[a]}$	$\tilde{H}_f = H_f\Delta\tilde{P}/\tilde{P}_0$	Planar-film coalescence kernel (1/s)
H_p	$\tilde{H}_p^{[a]}$	$\tilde{H}_p = H_p\Delta\tilde{P}/\tilde{P}_0$	Differential-pressure coalescence kernel (1/s)
l			Convex factor in pressures addition
m	$\tilde{m}^{[a]}$	$\tilde{m} = m\tilde{M}_0$	Bubble mass classes (kg)
m_m	$\tilde{m}_m^{[a]}$	$\tilde{m}_m = m_m\tilde{M}_0$	Mass of bubble melt film (kg)
M	$\tilde{M}\ (\tilde{M}_0)^{[a]}$	$\tilde{M} = M\tilde{\rho}_{g0}\tilde{R}_0^3 = M\tilde{M}_0$	Scaled single bubble mass (kg), single bubble mass is $4\pi M/3$
$\dot{M}$	$\dot{\tilde{M}}^{[a]}$	$\dot{\tilde{M}} = \dot{M}\tilde{M}_0\Delta\tilde{P}/\tilde{P}_0$	Rate of bubble mass change (kg/s)
$\overline{M}$	$\widetilde{\overline{M}}^{[a]}$	$\widetilde{\overline{M}} = \overline{M}\tilde{M}_0$	Diffusion-related equilibrium manifold (kg)
$\mathcal{M}$	$\tilde{\mathcal{M}}^{[a]}$	$\tilde{\mathcal{M}} = \mathcal{M}\tilde{M}_0$	Total mass of bubbles (kg)
$\mathcal{N}$			Total number of bubbles
$\mathcal{N}_m$	$\tilde{\mathcal{N}}_m^{[a]}$	$\tilde{\mathcal{N}}_m = \mathcal{N}_m\tilde{M}_0$	Marginal mass distribution
$\mathcal{N}_v$	$\tilde{\mathcal{N}}_v^{[a]}$	$\tilde{\mathcal{N}}_v = \mathcal{N}_v\tilde{V}_0$	Marginal volume distribution
P	$\tilde{P}$	$\tilde{P} = P\tilde{P}_0$	Bubble pressure (Pa)
$\overline{P}$	$\widetilde{\overline{P}}^{[a]}$	$\widetilde{\overline{P}} = \overline{P}\tilde{P}_0$	Pressure-related equilibrium manifold (Pa)
P_a	$\tilde{P}_a\ (\tilde{P}_0)^{[a]}$	$\tilde{P}_a = P_a\tilde{P}_0$	Ambient pressure (Pa)
Q	$\tilde{Q}^{[a]}$	$\tilde{Q} = Q\tilde{V}_0\tilde{M}_0\Delta\tilde{P}/\tilde{P}_0$	Coalescence operator (kg m^3 s^{-1})
Q_-	$\tilde{Q}_-^{[a]}$	$\tilde{Q}_- = Q_-\tilde{V}_0\tilde{M}_0\Delta\tilde{P}/\tilde{P}_0$	Negative coalescence operator (kg m^3 s^{-1})
Q_+	$\tilde{Q}_+^{[a]}$	$\tilde{Q}_+ = Q_+\tilde{V}_0\tilde{M}_0\Delta\tilde{P}/\tilde{P}_0$	Positive coalescence operator (kg m^3 s^{-1})
r	$\tilde{r}^{[a]}$	$\tilde{r} = r\tilde{R}_0$	Distance from bubble center (m)
R	$\tilde{R}\ (\tilde{R}_0)$	$\tilde{R} = R\tilde{R}_0$	Single bubble radius (m)
$\dot{R}$	$\dot{\tilde{R}}^{[a]}$	$\dot{\tilde{R}} = \dot{R}\tilde{R}_0\Delta\tilde{P}/\tilde{P}_0$	Single bubble growth rate (m/s)
$S\ (S_0)$	$\tilde{S}\ (\tilde{S}_0)^{[a]}$	$\tilde{S} = S\tilde{R}_0$	Influence zone radius (m)
t	$\tilde{t}^{[a]}$	$\tilde{t} = t\tilde{P}_0/\Delta\tilde{P}$	Time (s)
t_f	$\tilde{t}_f^{[a]}$	$\tilde{t}_f = t_f\tilde{P}_0/\Delta\tilde{P}$	Timescale for inter-bubble film rupture (s)
t_p	$\tilde{t}_p^{[a]}$	$\tilde{t}_p = t_p\tilde{P}_0/\Delta\tilde{P}$	Timescale for inter-bubble film deformation (s)
v	$\tilde{V}^{[a]}$	$\tilde{V} = v\tilde{V}_0$	Bubble volume classes (m^3)
V	$\tilde{V}\ (\tilde{V}_0)$	$\tilde{V} = V\tilde{V}_0$	Single bubble volume (m^3)
$\dot{V}$	$\dot{\tilde{V}}^{[a]}$	$\dot{\tilde{V}} = \dot{V}\tilde{V}_0\Delta\tilde{P}/\tilde{P}_0$	Rate of bubble volume change (m^3/s)
$\mathcal{V}\ (\mathcal{V}_0)$	$\tilde{\mathcal{V}}\ (\tilde{\mathcal{V}}_0)^{[a]}$	$\tilde{\mathcal{V}} = \mathcal{V}\tilde{V}_0$	Total bubble volume (m^3)
w	$\tilde{w}^{[a]}$	$\tilde{w} = w\tilde{V}_0$	Influence zone volume classes (m^3)
$\mathcal{W}\ (\mathcal{W}_0)$	$\tilde{\mathcal{W}}\ (\tilde{\mathcal{W}}_0)^{[a]}$	$\tilde{\mathcal{W}} = \mathcal{W}\tilde{V}_0$	Total melt volume (m^3)
Y			Factor in Eq. (16)
z	$\tilde{z}^{[a]}$	$\tilde{z} = z\tilde{R}_0$	Inter-bubble distance (m)
z_1	$\tilde{z}_1^{[a]}$	$\tilde{z}_1 = z_1\tilde{R}_0$	Estimate 1 of inter-bubble distance (m)
z_2	$\tilde{z}_2^{[a]}$	$\tilde{z}_2 = z_2\tilde{R}_0$	Estimate 2 of inter-bubble distance (m)
z_f	$\tilde{z}_f$	$\tilde{z}_f = z_f\tilde{R}_0$	Critical inter-bubble distance (m)
$\alpha\ (\alpha_0)$			Porosity (volume fraction)
β			Scaling exponent
Γ	$\tilde{\Gamma}^{[a]}$	$\tilde{\Gamma} = \Gamma\tilde{V}_0\Delta\tilde{P}/\tilde{P}_0$	Volume growth rate (m^3/s)
δm	$\delta\tilde{m}$	$\delta\tilde{m} = \delta m\tilde{M}_0$	Bubble mass increment (m)
δv	$\delta\tilde{v}$	$\delta\tilde{v} = \delta v\tilde{V}_0$	Bubble volume increment (m)
ε			Scaling constant
η	$\tilde{\eta}^{[a]}$	$\tilde{\eta} = \eta\tilde{\eta}_{m0}$	Effective magma viscosity (Pa s)
η_m	$\tilde{\eta}_m\ (\tilde{\eta}_{m0})$	$\tilde{\eta}_m = \eta_m\tilde{\eta}_{m0}$	Melt viscosity (Pa s)
Θ_D			Diffusion parameter
Θ_V			Viscous parameter
Λ_{ij}	$\tilde{\Lambda}_{ij}^{[a]}$	$\tilde{\Lambda}_{ij} = \Lambda_{ij}\tilde{V}_0^i\tilde{M}_0^j$	Moments of the distribution
ρ_g	$\tilde{\rho}_g\ (\tilde{\rho}_{g0})$	$\tilde{\rho}_g = \rho_g\tilde{\rho}_{g0}$	Gas density (kg/m^3)
ρ_m	$\tilde{\rho}_m$	$\tilde{\rho}_m = \rho_m\tilde{\rho}_{g0}$	Melt density (kg/m^3)
Σ	$\tilde{\Sigma}$	$\tilde{\Sigma} = \Sigma\tilde{R}_0\tilde{P}_0/2$	Surface tension (N m)
τ	$\tilde{\tau}^{[a]}$	$\tilde{\tau} = \tau\tilde{P}_0/\Delta\tilde{P}$	Time from t to t_f (s)
Ψ	$\tilde{\Psi}^{[a]}$	$\tilde{\Psi} = \Psi\tilde{M}_0\Delta\tilde{P}/\tilde{P}_0$	Mass growth rate (kg/s)
Ω			Dirac mass
	$\tilde{g}$		Gravity acceleration (9.81 m/s^2)
	$\tilde{G}_1^{[a]}$		H$_2$O molar mass (1.8 × 10^{-3} kg/mol)
	$\tilde{G}_2^{[a]}$		Universal gas constant (8.3144 J/mol/K)
	$\tilde{T}^{[a]}$		Temperature (K)
	$\delta\tilde{R}$		Bubble radius increment (m)

Table 1 (*continued*)

Dimensionless symbol	Dimensional symbol	Conversion	Variable
	$\Delta\tilde{P}$		Decompression rate (Pa/s)
Sub/superscripts			
'			Second bubble in coalescence relationships
^			Bubble resulting from a coalescence event
i,j			Indices

^a Only used in Table S1.

$$\dot{M} = \frac{3\rho_m}{\Theta_D} F(t,R) \tag{2}$$

$$\Theta_V = \frac{4\tilde{\eta}_{m0}\Delta\tilde{P}}{\tilde{P}_0^2} \quad \text{and} \quad \Theta_D = \frac{\Delta\tilde{P}\tilde{R}_0^2}{\tilde{D}_0\tilde{P}_0} \tag{3}$$

$$P_a(t) = 1 - t \tag{4}$$

$$P = M/R^3 \tag{5}$$

$$F(t,R) = \left(r^2 D \frac{\partial C}{\partial r}\right)_{r=R} \tag{6}$$

$$\frac{\partial C}{\partial t} + \frac{R^2 \dot{R}}{r^2}\frac{\partial C}{\partial r} = \frac{1}{\Theta_D r^2}\frac{\partial}{\partial r}\left(r^2 D \frac{\partial C}{\partial r}\right) \tag{7}$$

$$C(t,R) = C_H\sqrt{P} \quad \text{and} \left(\frac{\partial C}{\partial r}\right)_{r=s} = 0 \tag{8}$$

$$S^3 = R^3 + S_0^3 \tag{9}$$

$$C_T = \frac{M + C_0 S_0^3 \rho_m}{M + S_0^3 \rho_m} \tag{10}$$

$$\alpha(t) = (R/S)^3 \tag{11}$$

$$\eta = \eta_m(R)\left[1 - \frac{\eta_m(S)}{\eta_m(R)}\alpha - \frac{R^3}{\eta_m(R)}\int_R^S \frac{d\eta_m(r)}{dr}\frac{1}{r^3}dr\right] \tag{12}$$

where ρ_m is the melt density, Σ is the surface tension between the gas and the melt, $P = P(t)$ is the bubble pressure as a function of time, $P_a(t)$ is the ambient (melt) pressure, F is the volatile flux between melt and bubble, $C = C(r,t)$ is the volatile concentration in the melt surrounding the bubble, C_0 is the initial melt water content, C_T is the total water content, r is the distance from the bubble center, D is the H_2O diffusivity in the melt, S_0^3 is the volume occupied by the melt surrounding a bubble of radius zero, α is the bubble volume fraction, η is the effective magma viscosity, and $\eta_m = \eta_m(C(r,t))$ (shortened to $\eta_m(r)$) is the melt viscosity, which depends on melt composition, temperature, and melt water content at each radial position. The two relaxation parameters Θ_V and Θ_D are imposed by the scaling and respectively account for viscosity and diffusion. They depend on the dimensional initial values of melt viscosity, $\tilde{\eta}_{m0}$ (Pa s), ambient pressure, $\tilde{P}_0$ (Pa), bubble radius, $\tilde{R}_0$ (m), H_2O diffusivity in melt, $\tilde{D}_0$ ($m^2 s^{-1}$), and on the constant decompression rate, $\Delta\tilde{P}$ (Pa s^{-1}). Finally, $C_H = \tilde{K}_H\sqrt{\tilde{P}_0}$ is a dimensionless solubility factor, where $\tilde{K}_H$ ($Pa^{-1/2}$) is the dimensional Henrian constant.

Physically, Eq. (1) states that the time evolution of a bubble radius (or volume $V = R^3$) is governed by the difference between the gas pressure and the melt pressure corrected by surface tension. Eq. (2) is the differential version of mass conservation, which states that the change in bubble mass is equal to the mass of volatile diffusing between the melt and the bubble. The relaxation parameters Θ_V and Θ_D (Eq. (3))

can vary by several orders of magnitude and quantify viscous ($\Theta_D \ll \Theta_V$), diffusive ($\Theta_V \ll \Theta_D$), or equilibrium ($\Theta_D \sim \Theta_V$) growth regimes (Lensky et al., 2004). In the viscous regime the bubble–melt system is at the chemical equilibrium when $\Theta_D \ll 1$; in the diffusion regime the system is at the mechanical equilibrium when $\Theta_V \ll 1$; and in the equilibrium regime the system is at the thermodynamical equilibrium when $\Theta_D \ll 1$ and $\Theta_V \ll 1$. It has been numerically shown that computational times are very long when both relaxation parameters converge to zero (Forestier-Coste et al., 2012).

Eq. (4) states that the ambient pressure is linearly decreasing and eventually reaches a final value. The main volatile is water and, because the ideal gas law is assumed (Eq. (5)), the ambient pressure should remain between atmospheric and ~200 MPa. In Eq. (6) the flux $F(t,R)$ is defined by means of the volatile concentration in the melt surrounding the bubble, $C = C(r,t)$, which is given by the advection–diffusion Eq. (7). The left-hand side of Eq. (7) is an advection term that takes into account the fact that the bubble edge moves with a radial velocity given by $\dot{R}R^2/r^2$ because of melt incompressibility. The right-hand side describes the radial diffusion of dissolved water in the melt shell. The diffusion coefficient, D, is a function of melt composition, melt water content, ambient pressure, and temperature (e.g., Ni and Zhang, 2008). The left boundary condition in Eq. (8) asserts that the water content at the bubble edge is given by the solubility law and the right boundary condition in Eq. (8) states that at the outer edge ($r = S$) of the melt shell the concentration flux is null. Eq. (9) stipulates that the volume of the influence region, S^3, is constant in time and Eq. (10) ensures the conservation of the total water content, C_T. Eq. (11) gives the magma porosity, which is the fraction of volume occupied by the bubbles with respect to the total volume. Finally, Eq. (12) formulates the effective viscous resistance that the magma presents to a single bubble, which is a function of the proximity of the other bubbles and of the melt viscosity. Melt viscosity, η_m, depends on melt composition, temperature, and melt water content, C (e.g., Hess and Dingwell, 1996). It follows the variation of C from the inner to the outer part of the melt shell (Lensky et al., 2001).

The temperature, which enters into the ideal gas law (Eq. (5)), is assumed constant. Generalization to variable temperature is possible, but goes beyond the aim of this work. Both monodisperse and polydisperse numerical resolutions presented herein are thus isothermal, although we note that slow changes could be approximated by updating the temperature value at each simulated time step without changing the other aspects of the numerical resolutions. Finally, the kinetics of nucleation are not taken into account because the bubble population is assumed to pre-exist (i.e. there is an initial bubble radius $\tilde{R}_0$).

3. Results

3.1. Improvements on the monodisperse model

In order to diminish computational costs, we want to avoid the coupling with the advection–diffusion Eq. (7) in Eq. (2). We first note that Eq. (1) can be written in the form:

$$\dot{R} = \frac{R}{\eta\Theta_V}(P - \overline{P}) \tag{13}$$

where the equilibrium manifold $\overline{P} = \overline{P}(t,R)$ is given by:

$$\overline{P}(t,R) = P_a(t) + \frac{\Sigma}{R} \tag{14}$$

which corresponds to the mechanical equilibrium $\Theta_V \to 0$.

By analogy with the radius growth, Eq. (2) is replaced by:

$$\dot{M} = A \frac{D}{\Theta_D} (\overline{M} - M) \tag{15}$$

where A is a scaling variable and $\overline{M} = \overline{M}(R)$ is the equilibrium manifold defined by the chemical equilibrium case, that is when $\Theta_D \to 0$ (Eq. 43 in Forestier-Coste et al., 2012):

$$\overline{M}(R) = \frac{\left(-YC_H + \sqrt{Y^2 C_H^2 + 4R^3 YC_T}\right)^2}{4R^3} \tag{16}$$

where $Y = \rho_m S_0^3$ and C_T is the total dimensionless volatile concentration when the bubble radius is zero (Eq. 10). The accuracy of this simplification for different values of the relaxation parameters is shown in Section 3.4. These numerical comparisons indicate that the choice $A = 1$ yields excellent results. An implementation of this simplified flux is available in the software B-Growth, which is included as Supplementary data. B-Growth is a C++, open-source code that solves the full monodisperse system of Eqs. (1) to (12) following Forestier-Coste et al. (2012), and allows the user to select various simplifications of the full system, including Eqs. (15) to (16).

3.2. Coalescence kernels

Modeling a polydisperse bubble population opens the possibility of taking their interactions into account. In the case of gas bubbles in magmas, these interactions are driven by coalescence, which is the aggregation of two or more bubbles into a single larger bubble. Here we consider only instantaneous binary coalescence, which means that interactions take place only between two bubbles at a time, and the time needed for the created bubble to get back to a spherical geometry is instantaneous (i.e. the relaxation time is null). We thus neglect the formation of chains of coalescing bubbles, although this is an important and observed behavior (e.g., Burgisser and Gardner, 2005). Multiple coalescence and bubble chains may be studied using the framework we propose in a later time by considering for instance a new parameter characterizing the shape of the created bubble.

In order to mathematically describe the merging of bubbles, a coalescence kernel, H, has to be defined. Bubble dimensions are characterized by their volume, $V = R^3$, and mass, M. The kernel H corresponds to the rate of interaction between bubbles; hence it depends on time and on the bubble dimensions. It must be positive, $H = H(t,V,M,V',M') \geq 0$, and symmetric, $H(t,V,M,V',M') = H(t,V',M',V,M)$, which means that the interaction of a bubble of dimensions (V,M) with a bubble (V',M') must give the same result than the interaction of a bubble (V',M') with a bubble (V,M). We consider here three coalescence kernels. The first two are based on coalescence mechanisms proposed in Castro et al. (2012) for high-viscosity magmas where bubbles have vanishing relative velocities. The third one is based on a mechanism proposed in Lovejoy et al. (2004) for low-viscosity magmas where buoyancy confers relative velocities to neighboring bubbles of different sizes.

The two first mechanisms are functions of the distance between two neighboring bubbles. The monodisperse formulation approximately divides the melt into spherical melt shells that overlap in a way that the overlaps compensate the gaps (a.k.a. plateau borders, Proussevitch et al., 1993b) left between the shells (Proussevitch and Sahagian, 1998; Lensky et al., 2004). We use in Fig. 1 the same approximation for polydisperse systems. Both coalescence mechanisms assume that

not only melt shells but also bubbles are overlapping pairwise (Fig. 2B–C). Even if the thickness of the melt film trapped between the deformed bubble pair can be calculated by using the reasonable approximation that the melt shell thickness, S–R, is preserved all around the deformed bubble, the geometric configurations of Fig. 2B–C cannot be depicted rigorously in the kinetic model because the kinetic framework is based on a non-local, statistical description of the bubble size and mass distribution. Since this issue is linked to the broader, much more complex topic of maximum packing in polydisperse suspensions (e.g., Baranau and Tallarek, 2014), we present two simple solutions to calculate the inter-bubble distance, z. The most accurate one, $z = z_1$, estimates the inter-bubble distance while preserving melt shell overlap and a finite maximum packing. It is presented in Appendix B because of its lengthy algebraic formulation. A simpler form, $z = z_2$, can be expressed in the dimensionless terms of bubble volumes and magma porosity, Eq. (11), by:

$$z_2 = \left(V^{1/3} + V'^{1/3}\right)\left(\alpha^{-1/3} - 1\right). \tag{17}$$

This assumes that melt shells are touching so that $z_2 = S + S' - R - R'$ (Fig. 2A). It does not represent overlapping shells (Fig. 2A) and
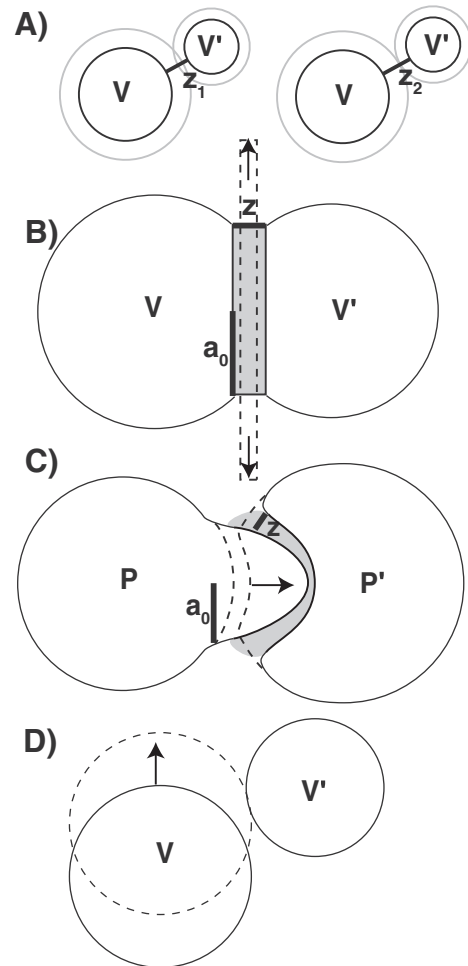

Fig. 2. Schematics of two coalescing bubbles of volume V and V'. A) Two configurations of bubble pairs: overlapping melt shells (left), and touching melt shells (right). Overlapping shells correspond to the arrangement depicted in Fig. 1, with z_1 being the inter-bubble distance. Touching melt shells yield Eq. (17) for the inter-bubble distance z_2. A) Coalescence by planar film thinning. Inter-bubble film has radius a_0 and thickness z. B) Coalescence by differential bubble pressure (P–P'). Inter-bubble film has radius a_0 and thickness z. C) Coalescence by bubble collision. Gray regions in A) and B) is where melt mass is conserved until film breakup and arrows indicate the main direction of motion of the considered feature.

overestimates z (i.e. maximum packing, $z_1 \to 0$, occurs when $\alpha \to 1$), but does not contain assumptions on the degree of polydispersity of the system (Appendix B).

The configuration of bubbles affected by the first mechanism, planar-film coalescence, is depicted in Fig. 2B. Planar-film coalescence was first described by Castro et al. (2012) for bubbles growing at identical rates. We release here this assumption as the growth rates of both bubbles are known. Assuming that the cylindrical shape of the melt film contained in the flat plane between two merging bubbles is conserved during the growth process just prior to coalescence, one can write in dimensionless form (Castro et al., 2012):

$$m_m(\tau) = \rho_m \pi z(\tau) a^2(\tau) \tag{18}$$

where τ is the time from the considered time, t, and the time at which coalescence occurs, t_f, $m_m(\tau)$ is the mass of the melt film, $z(\tau)$ is the distance between the bubbles, and $a(\tau)$ corresponds to the radius of the disc of the flat section of the bubbles, which is assumed to be the same for each of the two bubbles (Fig. 2). Assuming that the radius $a(\tau)$ can be approximated by a linear growth from the considered time until coalescence, $a(\tau) = a_0 + c\tau$, where a_0 is the initial radius given by:

$$a_0 = \epsilon(R + R')/2 \tag{19}$$

where $0 < \epsilon < 1$ is the ratio between bubble size and film size, and c is the rate at which the film thins off, which is given by the mean between the two growth rates: $c = (\dot{R} + \dot{R}')/2$.

Assuming that m_m is constant from t until t_f because of the high melt viscosity, solving $m_m(\tau) = m_m(t_f)$, where t_f is the final time at breakage when the film thickness reaches the critical value z_f, it is possible to calculate the time needed to reach the film breaking distance (Castro et al., 2012). The planar-film coalescence kernel, $H_f(V,M,V',M')$, is the rate of coalescence of the merging bubble couple, which we define as the inverse of t_f:

$$H_f\left(V, M, V', M'\right) = \frac{\left(V^{-2/3}\dot{V} + V'^{-2/3}\dot{V}'\right)}{3\varepsilon\left(V^{1/3} + V'^{1/3}\right)} \frac{\sqrt{z_f}}{\sqrt{z} - \sqrt{z_f}}. \tag{20}$$

The factor ε and the final distance at breakage, z_f, are constants determined by the physical characteristics of the melt and by experimental measurements. The distance between the two bubbles, z, is equal to either z_1 or z_2. Since all kernels must be ≥ 0, one has to ensure that H_f does not yield negative values. This can occur when at least one bubble shrinks, in which case H_f is set to zero during the numerical resolution. Another possibility is that the porosity is so large that $z < z_f$, in which case H_f is set to an arbitrary large value during the numerical resolution.

The configuration of bubbles affected by the second mechanism, differential-pressure coalescence, is depicted in Fig. 2B. Following Castro et al. (2012), the corresponding kernel is defined in dimensionless form as the inverse of the characteristic time for film deformation by stretching, t_p:

$$\frac{1}{t_p} = \frac{8a_0|P - P'|}{\Theta_V z \eta} \tag{21}$$

where a_0 and z are defined as for the planar-film kernel and $|P-P'|$ is the difference of pressure between the two merging bubbles, which can be computed thanks to the dimensionless ideal gas law ($P = M/V$). The differential-pressure kernel is thus:

$$H_p\left(V, M, V', M'\right) = \frac{4\varepsilon\left(V^{1/3} + V'^{1/3}\right)}{\eta\Theta_V z}\left|\frac{M}{V} - \frac{M'}{V'}\right|. \tag{22}$$

The third mechanism is the coalescence caused by bubble collision because of their relative velocities, which was proposed by Lovejoy et al. (2004) and is illustrated in Fig. 2D. Since their kernel is based on a probability distribution function of bubble per unit volume, we need to divide it (in dimensional form) by the initial volume, $\tilde{V}_0 = 4\pi\tilde{R}_0^3/3$, to make it compatible with our definition of the distribution function f (see Section 3.3). Using their Eqs. 9–11, setting their γ coefficient to $-2/3$, their efficiency coefficient to 1 (e.g., Berry, 1967), and using the Stokes terminal rise velocity of bubbles of size $\tilde{R}_0$ as the initial velocity, the dimensionless collision kernel, $H_c(V,V')$, becomes:

$$H_c\left(V, V'\right) = \frac{2\tilde{g}\tilde{\rho}_{g0}\tilde{R}_0}{3\pi\tilde{P}_0} \frac{(\rho_m - 1)}{\eta\Theta_V}\left(V^{1/3} + V'^{1/3}\right)^2\left|V^{-2/3} - V'^{-2/3}\right| \tag{23}$$

where the fraction on the left-hand side regroups the dimensional parameters, which include the constant of the acceleration of gravity, $\tilde{g}$.

To conclude the description of the coalescence phenomena, the rules linking the dimensions (V,M) and (V',M') of two coalescing bubbles to those $(\hat{V}, \hat{M})$ of the created bubble must be determined. It is physically natural to assume that masses sum up, but this is not the case for volumes. Unlike modeling usually done when considering polymers, for which mass and volume are equivalent (e.g., Escobedo et al., 2004; Carrillo et al., 2008), in our model these two variables are independent. Since volumes combine as a complex function of pressure re-equilibration after coalescence, we assume, as a first approach, that they actually sum up. Thus volumes and masses verify $\hat{V} = V + V'$ and $\hat{M} = M + M'$. As a consequence of the ideal gas law holding in each bubble, the pressure $\hat{P}$ in the created bubble is given by a convex combination of the pressures in the two coalescing bubbles P and P': $\hat{P} = lP + (1 - l)P'$ with $l = V/(V + V')$.

3.3. The kinetic model

We describe the evolution of a polydisperse population of gas bubbles in magma growing by decompression, exsolution, and coalescence at a statistical level by the means of a kinetic, Smoluchowski-type equation. Considering the monodisperse model described in Section 2, we define that each bubble of the polydisperse suspension has three characteristic variables: the volume, v, the mass, m, and the volume of the melt shell, w. Instead of Eq. (11) the porosity α should be computed by:

$$\alpha(t) = \frac{\mathcal{V}}{\mathcal{V} + \mathcal{W}} \tag{24}$$

where $\mathcal{V} = \mathcal{V}(t)$ is the total volume occupied by the bubbles and $\mathcal{W}$ is the volume occupied by the melt. Knowing the initial porosity, α_0, the initial bubble volume, $\mathcal{V}_0$, and under the assumption that the volume of melt is constant, as follows from Eq. (24), $\mathcal{W} = \mathcal{W}_0$ with $\mathcal{W}_0$ given by:

$$\mathcal{W}_0 = \frac{1 - \alpha_0}{\alpha_0}\mathcal{V}_0. \tag{25}$$

In analogy with Eq. (25), w is linked to the porosity, α, and to the bubble volume by:

$$w = (\alpha^{-1} - 1)v. \tag{26}$$

Therefore, the number of variables in the distribution function f is reduced from four to three: $f = f(t,v,m)$. From a physical point of view, definition (26) says that bubbles occupying the same volume v have the same influence region w. This assumption may be relaxed at a heavy computational cost because the numerical resolution of the time evolution of f would involve four variables and coalescence kernels would involve three variables instead of two. Note also that by Eq. (9), the growth rate of the influence region volume is zero. Since bubbles grow by expansion and coalescence and since the volumes of the

influence region are constant, the distribution function $f(t,v,m)$ must satisfy the following kind of kinetic equation:

$$\frac{\partial f}{\partial t} + \frac{\partial}{\partial v}(\Gamma f) + \frac{\partial}{\partial m}(\Psi f) = Q(f). \tag{27}$$

The left-hand side in Eq. (27) is a conservative equation that describes the evolution by decompression and exsolution of the set of bubbles, where the two growth rates for volumes and masses are respectively defined by the non-linear functions $\Gamma = \Gamma(t,v,m)$ and $\Psi = \Psi(t,v,m)$:

$$\Gamma(t,v,m) = \frac{3}{\eta \Theta_V}\left(m - (1-t)v - \Sigma v^{2/3}\right) \tag{28}$$

$$\Psi(t,v,m) = \frac{D}{\Theta_D}\left(\frac{\left(-C_H \rho_m w + \sqrt{C_H^2 \rho_m^2 w^2 + 4\rho_m v w C_T}\right)^2}{4v} - m\right) \tag{29}$$

where w is defined by Eq. (26) and C_H, ρ_m, Σ, C_T, D, Θ_V and Θ_D have been introduced in Section 2. Note that Eqs. (28) and (29) are deduced from Eqs. (13) and (15), respectively.

The right-hand side in Eq. (27) describes bubbles coalescence by means of the Smoluchowski continuous coalescence operator:

$$Q(f)(t,v,m) = Q_+ - Q_-$$

$$Q_+ = \frac{1}{2}\int_0^m \int_0^v H\left(t, v', m', v-v', m-m'\right) f\left(t, v', m'\right) f\left(t, v-v', m-m'\right) dv' dm'$$

$$Q_- = f(t,v,m)\int_0^\infty \int_0^\infty H\left(t, v', m', v, m\right) f\left(t, v', m'\right) dv' dm' \tag{30}$$

where H is the coalescence kernel defined by Eqs. (20), (22), or (23), and v and m are integration variables. The Q_+ term is the gain that counts the bubbles created by the coalescence of a bubble of dimensions (v,m) and one of dimensions (v',m'). The Q_- term is the loss that counts the bubbles of dimensions (v,m) disappearing by coalescence with bubbles of any other dimensions.

Nucleation is not taken into account in the kinetic model, so Eq. (27) is fed by an initial condition $f_0 = f_0(0,v,m) \geq 0$ describing the distribution of bubbles at the initial time $t = 0$ in the phase space Π $[0,V_{max}] \times [0,M_{max}]$. Note that the initial condition f_0 given by the experimental measures is formally defined as a sum of Dirac masses although it is measured as a discrete size distribution. In other words, if $\mathcal{D}_{i,j}$ is the initial number of bubbles measured per class of volume and mass (i.e. $\mathcal{D}_{2,3} = 4$ means that there are 4 bubbles of mass v_2 and mass m_3), then $f_{0,i,j} = (\mathcal{D}_{i,j}\Omega_{i,j})/(\delta v_i \delta m_j \sum_{l,k}\mathcal{D}_{k,l})$, where $\Omega_{i,j}$ is the Dirac mass such that $\Omega_{i,j} = 1$ if $i = j$ and zero otherwise, δv_i and δm_j are the respective dimensionless volume and mass bin sizes, and $\sum_{l,k}\mathcal{D}_{k,l}$ is the total number of bubbles before normalization. Using dimensional volume and mass classes, $\tilde{v}$ and $\tilde{m}$, $f_{0,i,j} = (\mathcal{D}_{i,j}\Omega_{i,j}\tilde{V}_0\tilde{M}_0)/(\delta\tilde{v}_i\delta\tilde{m}_j\sum_{l,k}\mathcal{D}_{k,l})$. The numerical phase space domain is bounded both in v and m, and we impose no flux conditions for the larger values of v and m. On the other hand, for $v = 0$ or $m = 0$ we note that the respective drifts are coming into the domain (see Eqs. (13) and (15)), so it suffices to set the initial condition $f_0 = 0$ for $v = 0$ or $m = 0$.

The moments of the distribution function $f(t,v,m)$ yield dimensionless macroscopic quantities of physical interest such as the total number of bubbles, $\mathcal{N}(t)$, the total (normalized) volume of bubbles, $\mathcal{V}(t)$, the mass of bubbles, $\mathcal{M}(t)$, and the porosity, $\alpha(t)$, by applying Eq. (24). Let i and j be two integers, then the moments $\Lambda_{i,j} = \Lambda_{i,j}(t)$ of order $i + j$ of f are given by:

$$\Lambda_{i,j} = \int_0^\infty \int_0^\infty v^i m^j f(t,v,m)dv\,dm. \tag{31}$$

The zeroth order moment is the total number of bubbles:

$$\mathcal{N}(t) = \Lambda_{0,0} = \int_0^\infty \int_0^\infty f(t,v,m)\,dv\,dm. \tag{32}$$

The first order moment for $i = 1$ and $j = 0$ is the total bubble volume:

$$\mathcal{V}(t) = \Lambda_{1,0} = \int_0^\infty \int_0^\infty v\,f(t,v,m)\,dv\,dm. \tag{33}$$

The first order moment for $i = 0$ and $j = 1$ is the total bubble mass:

$$\mathcal{M}(t) = \Lambda_{0,1} = \int_0^\infty \int_0^\infty m\,f(t,v,m)\,dv\,dm. \tag{34}$$

Since the left-hand side of Eq. (27) is a conservation equation, the number of bubbles must be conserved when neglecting coalescence, that is $\mathcal{N}(t) = \mathcal{N}(0)$. This can be proved by integrating Eqs. (27) and (32) over the interval $[0,t]$. On the other hand, the first-order moments, $\Lambda_{1,0}$ and $\Lambda_{0,1}$, must be conserved when neglecting the expansion terms in Eq. (27), which means that bubble volumes and masses are conserved: $\mathcal{V}(t) = \mathcal{V}(0)$ and $\mathcal{M}(t) = \mathcal{M}(0)$ (Lovejoy et al., 2004). For some kernels H, this occurs only for a finite time, a phenomenon called gelation (e.g., Filbet and Laurençot, 2004; Forestier-Coste and Mancini, 2012). If the first-order moments are constant in time, then any linear combination of them will be constant in time, too. Since the first-order moments are conserved by the coalescence operator, the porosity may change only by the influence of the left-hand side of Eq. (27). This implies that the numerical comparison of the porosity computed by the monodisperse model and that computed by the kinetic equation must be identical, unless gelation occurs. Note that at a discrete level it will not be possible to conserve both first-order moments (Forestier-Coste and Mancini, 2012; Appendix A).

For practical and comparison purposes, it is convenient to report size distributions by collapsing one of the dimensions. The dimensionless, marginal distributions in volume, $\mathcal{N}_v$, and mass, $\mathcal{N}_m$, are given by:

$$\mathcal{N}_v(t,v) = \int_0^\infty f(t,v,m)\,dm \tag{35}$$

$$\mathcal{N}_m(t,m) = \int_0^\infty f(t,v,m)\,dv \tag{36}$$

3.4. Application to decompressing rhyolite

We use data from isothermal decompression experiments of rhyolitic melt (Burgisser and Gardner, 2005). Briefly, these experiments consisted in placing various samples of the starting natural rhyolite in sealed capsules with water, heating them under high pressure for several days in order to ensure water saturation. Samples were then quenched and removed from the pressure vessel. Capsules were opened to extract the hydrated samples, which were reloaded into capsules without water, but with either silicate glass powder or MgO powder to serve as a sink for expelled water during decompression, allowing open-degassing conditions. Each capsule was then re-pressurized and reheated at the hydration conditions for a few minutes before an applied sudden decompression at constant temperature nucleated small bubbles (mean radius ≪ 10 μm). The sample was maintained at that pressure until bubbles reach thermodynamical equilibrium. Then several decompression steps are applied rhythmically until a final pressure is reached, which approximates a constant decompression rate. The sample is rapidly cooled down when the final pressure is reached so as to quench the bubbles.

At the end of the experiment, samples were cut and analyzed in thin section to measure the number and sizes of the created bubbles. We use here bubble size distributions separated in regular classes of radius. An experimental series is defined by several samples quenched at progressively lower final pressures under identical starting conditions and decompression rate. The nucleation step, however, cannot be

reproduced exactly from an experiment to another. As a result, samples have slightly different initial bubble size distributions. These differences, although visible on the tabulated data, are smaller than the changes induced by coalescence and growth.

In a first approach coalescence is neglected, only the expansion model is considered. The validation is carried out by comparing the outputs of 77 different computations (Fig. 3). Eleven initial conditions (Θ_V and Θ_D pairs) were explored by varying the decompression rate from 10^4 to 10^{-4} MPa/s and setting the temperature to either 750 or 850 °C (Fig. 3A). Other initial conditions are as follows: the porosity is $\alpha_0 = 10\%$, the volatile concentration is $C_0 = 3.44$ wt%, the initial pressure is $\tilde{P}_0 = 100$ MPa, the surface tension is $\tilde{\Sigma} = 0.1$ N m, the melt density is $\tilde{\rho}_m = 2400$ kg m^{-3}, the solubility constant is $\tilde{K}_H = 3.44 \times 10^{-6}$ Pa$^{-1/2}$, the melt viscosity $\tilde{\eta}_m$ follows the Hess and
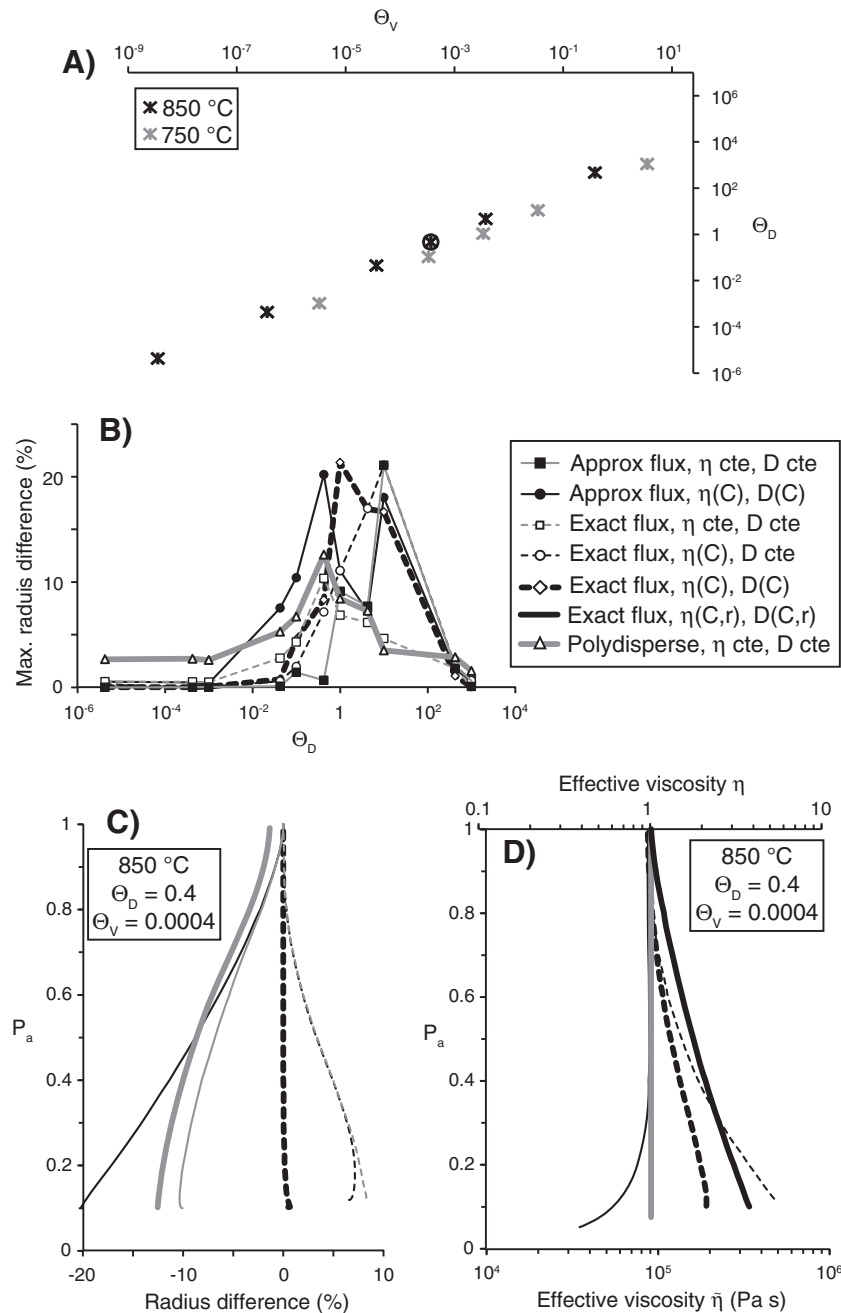
Fig. 3. Comparison between solutions of the monodisperse model and the kinetic polydisperse model. Runs were done by varying the decompression rate from 10^4 to 10^{-4} MPa/s and setting the temperature of the rhyolitic melt to either 750 or 850 °C. A) Values of the relaxation parameters Θ_V and Θ_D for the 11 cases were explored. Each case was run with 6 versions of the monodisperse model and one version of the polydisperse model to illustrate how various assumptions on the behavior of the effective viscosity and water diffusivity affects the evolution of bubble radius. Circled case is shown in more details in panels C and D. B) Maximum difference between the monodisperse runs with exact flux and fully varying viscosity and diffusivity across the melt shell (label "Exact flux, $\eta(C,r)$, $D(C,r)$") and the other versions (labels "η cte", "D cte", "$\eta(C)$", and "$D(C)$" respectively mean constant effective viscosity, constant diffusivity, variable effective viscosity with constant C across the melt shell, and variable diffusivity with constant C across the melt shell) as a function of Θ_D. C) Example of how the radius difference changes as a function of dimensionless ambient pressure (P_a) for one run (850 °C, $\Theta_D = 0.4$, $\Theta_V = 4 \times 10^{-4}$, circled in panel A). The maximum absolute value of each curve is reported in B) (e.g., 10% for the monodisperse run with constant η and D). D) Example of how the effective viscosity changes as a function of dimensionless ambient pressure (P_a) for the same run as C).

Dingwell (1996) relationship, water diffusivity, $\widetilde{D}$, follows the Ni and Zhang (2008), Eq. (13) relationship, and the scaling value $\widetilde{R}_0 = 10$ μm is defined as the mean bubble radius over all the measured radii at initial time. The initial distribution of the kinetic model reads $f_{0ij}\delta v_i \delta m_j = \Omega_{41\,41}$ where $\Omega_{i\,j}$ is a Dirac mass such that $\Omega_{i\,j} = 1$ if $i = 41$ and $j = 41$, zero otherwise. This function corresponds to an initial population of bubbles with all the same radius and mass. We choose $N = 150$ discretization points for the numerical mesh in v and m and the uniform radius step is $\delta\widetilde{R} = 0.25$ μm starting at 0 μm (see Appendix A). Calculations stopped when either atmospheric pressure or 75 vol% porosity was reached. These initial conditions approach those at the start of the decompression experiments in Burgisser and Gardner (2005) when $10^{-2} < \Theta_D < 10$ and $10^{-7} < \Theta_V < 10^{-3}$. The other values of Θ_D and Θ_V cover a range broader than that expected for the shallow ascent of a rhyolitic melt (Burgisser and Degruyter, 2015), which confers a general character to this validation.

Each set of initial conditions was run with 6 versions of the monodisperse model and one version of the polydisperse model. Each monodisperse version has different build-in assumptions on the behavior of the effective viscosity and water diffusivity. The reference version uses the full monodisperse equation system (1–12) with variable effective viscosity and diffusivity across the melt shell (Forestier-Coste et al., 2012). Two versions solve the same full system but assume that the diffusivity remains at its initial value and either that effective viscosity remains at its initial value, or that effective viscosity is calculated using the value of melt water content given by Eq. (10) with $C = C_0$ (i.e. $C = C_T + M(C_T-1)/(S_0^3 \rho_m)$). This simplification of the effective viscosity has for effect to ignore the last term in brackets in Eq. (12). The fourth version solves the same system but calculates both diffusivity and effective viscosity using only the value of melt water content at the bubble edge. The two last versions use the simplified flux developed herein (i.e. replacing Eqs. (2) and (6)–(8) by Eqs. (15)–(16) and assume either that diffusivity and effective viscosity remain at their initial values, or that they are calculated using the value of melt water content at each pressure step given by Eq. (10) with $C = C_0$. The various assumptions of these six versions can all be selected in the software B-Growth (Supplementary Data), which was used to produce the resulting 66 monodisperse runs.

Fig. 3B shows the difference in bubble radius between the reference version and the other monodisperse versions as a function of Θ_D. For each value of Θ_D, the corresponding value of Θ_V can be read on Fig. 3A. In other words, the succession of points along a given curve of Fig. 3B corresponds to that along the Θ_D axis of Fig. 3A. Differences are for each run the maximum value over the whole course of the run. Overall, differences are <3% if $\Theta_D < 10^{-2}$ and $\Theta_D > 10^3$ while differences reach 20% in the intermediate range. The larger differences do not arise with the most restrictive set of assumptions (D and η constant). Chernov et al. (2014) proposed a simple parameter, $(\sqrt{P} - \sqrt{P_a})C_H \rho_m/\rho_g$, that quantifies the degree of super-saturation of the melt. If this parameter is >~10^{-2}, steady-state simplifications of Eq. (8) have a low degree of accuracy. Figure S1 suggests this happens for the second half of the decompression of runs with $\Theta_D > 1$. Fig. 3B, however, suggests that the various approximations become more accurate as Θ_D increases despite larger degrees of super-saturation. This situation arises because, as explored in more details by Proussevitch and Sahagian (1998), the combined effect of each simplification is quite complex. They can be understood by focusing on a case with large differences between the runs ($\Theta_D = 0.4$ at 850 °C, circle on Fig. 3A). Fig. 3C and D show respectively the evolution of radius difference and η with ambient pressure for that case. The reference version shows that the effective viscosity increases by a factor 3 during the run because of the combined effects of decreasing diffusivity and higher melt viscosity near the bubble edge (Lensky et al., 2001). Ignoring variable viscosity in the melt shell slightly underestimates the effective viscosity but does not affect the estimation

of bubble radius (thick, black, dashed curves in Fig. 3C and D). At large Θ_D, melt water content remains high during decompression, such that η is mostly affected by porosity increase. When diffusivity decreases during decompression, this phenomenon is accentuated and η can decrease at low pressure, such as with the simplified-flux model with variable η and D (thin continuous curves in Fig. 3C and D). Overall, these competing effects interact in such a way that assuming constant η and D in the full system leads to radius differences of at most ~20%. Fig. 3B also suggests that the simplification of the flux with constant η and D is acceptable as it brings these differences to a maximum of ~10%.

Considering the results of Fig. 3 for the monodisperse model, the polydisperse model was run in a version that assumes $Q = 0$, constant initial diffusivity, and constant effective viscosity. For comparison purposes, the evolution of the size and mass distribution, f, is represented in Fig. 3 by the median bubble radius. The polydisperse runs and the simplified-flux runs with constant D and η yield similar radius evolutions with a slight (~1.25%), nearly constant difference over all values of Θ_D (Fig. 3B). This is due to the discrete nature of the bins in the polydisperse model. It corresponds to half the bin size and could be made negligible by selecting bins limits that exactly frame the value of the initial 10 μm radius, that is bins $\widetilde{R} = (.., 9.875, 10.125, 10.375,..)$ instead of $\widetilde{R} = (.., 9.75, 10, 10.25,..)$. Such binning was not attempted as it would make both monodisperse and polydisperse model curves undistinguishable at the scale of Fig. 3, thereby weakening its clarity.

The numerical solution of the kinetic model with constant diffusivity and effective viscosity is now compared with experimental data that features both growth and coalescence (Burgisser and Gardner, 2005; Castro et al., 2012). The initial size distribution from sample PPE4 contains 220 bubbles, which were sampled in regular intervals of $\delta\widetilde{R} = 2.5$ μm. The corresponding initial condition reads in the kinetic framework: $f_{0ij}\delta v_i \delta m_j = \mathcal{D}_i \Omega_{ij}/220$ where $\mathcal{D}_i = (1,2,7,8,8,12,15,14,23,25,21,25,21,15,12,5,5,0,0,1)$ and Ω_{ij} are Dirac masses such that $\Omega_{ij} = 1$ if $i = j$ and zero otherwise. The decompression rate is $\Delta\widetilde{P} = 0.025$ MPa s^{-1}, the viscosity is $\widetilde{\eta}_{m0} = 1.5 \times 10^6$ Pa s, the temperature is 825 °C, the surface tension is $\widetilde{\Sigma} = 0.1$ N m, the melt density is $\widetilde{\rho}_m = 2354$ kg m^{-3}, the diffusion coefficient is $\widetilde{D}_0 = 6.95 \times 10^{-12}$ m^2 s^{-1}. Initial values specific to PPE4 are: the volatile concentration is $C_0 = 1.92855$ wt.% (a high precision limits initial radii oscillations), the porosity is $\alpha_0 = 31.43\%$, the ambient pressure is $\widetilde{P}_0 = 40$ MPa, the solubility constant is $\widetilde{K}_H = 3.44 \times 10^{-6}$ Pa$^{-1/2}$, and the scaling radius is $\widetilde{R}_0 = 38.5$ μm. Simulations kept the same sampling interval as that of the initial conditions with N between 150 and 300 discretization points. Experiments PPE7, PPE10, and PPE11, to which simulations runs are compared, were quenched at ambient pressures of 34, 28, and 24 MPa, which correspond to dimensionless times $t = 0.15, 0.3,$ and 0.4, respectively.

The distributions of PPE7 and PPE10 contain respectively 48 and 60 bubbles, whereas PPE11 contains 209 bubbles. These small numbers (<100) are caused by coalescence, which creates bubbles of a size comparable to that of the sample. This situation has two consequences. First, we found preferable to resample both the simulations results and the experimental data to intervals of 12.5 μm for comparison. Second, it precludes the comparison between experimental and simulated porosities. Coalescence led some large bubbles to connect with the sample outer surface, thereby leaving the sample and causing the porosity measure to be underestimated and unreliable. Sample PPE10, for instance, as a measured porosity of 30.6%, which is below the starting porosity of PPE4 (31.4%), and hence also below that of predicted by the three simulations (~61%).

A short while into the simulations (around $t \sim 0.1$), time steps became vanishingly small (<10^{-10}), which caused prohibitively long calculation times (on the order of several months). These small time steps are due to numerical diffusion from bubble-bearing bins, $f(t,v,m) \gg 0$, into near-zero bins (in practice between machine precision and

10^{-20}). A limiting condition so that $f(t,v,m) \geq 10^{-20}$ was thus added at the end of each iteration. This kept the time steps above 10^{-5} and total simulation times between 1 and 10 h on an ordinary PC, depending on the coalescence kernel. We tested the accuracy loss by graphically superimposing the solutions with and without the limiting condition and found it to be negligible. A more rigorous estimate is hindered by the fact that time steps are not identical between these test runs. It can nevertheless be stated that the percent differences on the marginal with respect to the volume caused by this rounding are of the same order ($10^{-6} - 10^{-7}\%$) as those caused by unequal time steps.

Fig. 4 shows the 2D distribution function in v and m for the initial data (sample PPE4) and the final time $t = 0.4$ in the case of planar-film, H_f, and differential-pressure coalescence, H_p. Since no initial distribution in m was available from experimental data, an approached distribution ignoring the contribution of surface tension, $m = v$, was used instead for t = 0. The resulting initial distribution (Fig. 4A) is thus shifted from the equilibrium manifold defined by the chemical and mechanical equilibria and given by $m = (1-t)v + \Sigma v^{2/3}$ (Forestier-Coste et al., 2012). The distribution functions at $t = 0.4$ (Fig. 4B–C) both
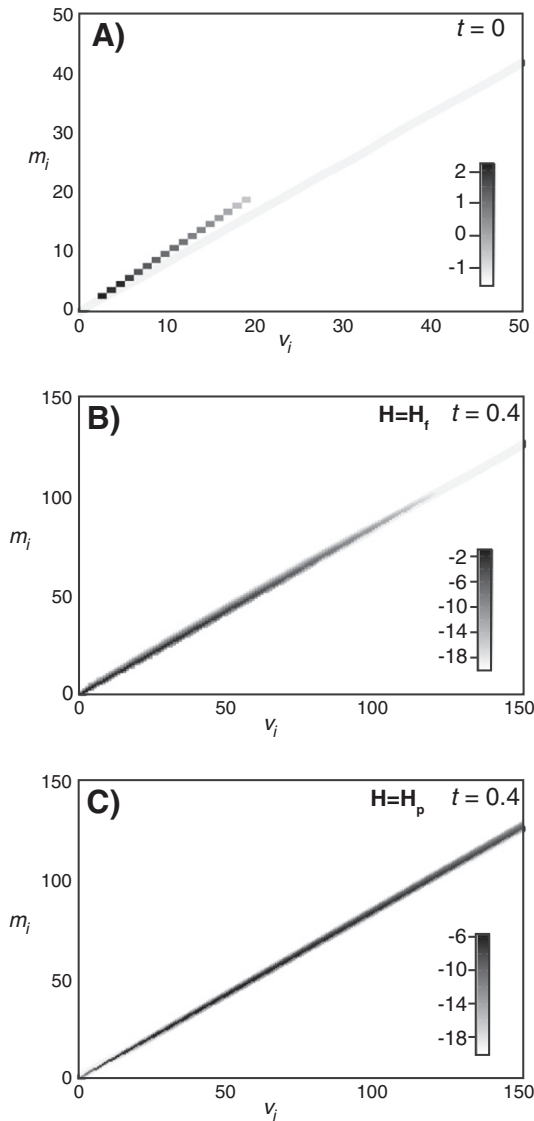

Fig. 4. Bi-dimensional solutions for coalescence runs. Axes are graduated in mesh units and gray scales indicate $\log_{10}$ values of f in dimensionless units (Table 1). Thick gray lines are the equilibrium solutions. A) Initial condition at $t = 0$. B) Planar-film coalescence at $t = 0.4$ with $z = z_1$ ($H = H_f$). C) Differential-pressure coalescence with $z = z_1$ at $t = 0.4$ ($H = H_p$).

concentrate on the equilibrium manifold, which is consistent with the growth regime prevailing during this experimental set ($\Theta_V = 9.4 \times 10^{-5}$ and $\Theta_D = 1.3 \times 10^{-1}$).

Fig. 5 shows the size distributions from six simulations compared to the experimental data. The first run has no coalescence ($H = 0$, Fig. 5A) and the second run assumes collision coalescence ($H = H_c$, Fig. 5B). In the third and fourth runs, coalescence occurs by planar-film thinning, H_f, with either $z = z_1$ (Fig. 5C), or $z = z_2$ (Fig. 5D). In the fifth and sixth runs, coalescence occurs by differential bubble pressure, H_p, with either $z = z_1$ (Fig. 5E), or $z = z_2$ (Fig. 5F). The vertical axis is the cumulated volume fraction of each class size (i.e. the bubble volume times the number of bubbles in the marginal distribution with respect to the volume, $\mathcal{N}_v \times v$, Eq. (35)). The jagged appearance of the experimental distributions is due to the fact that intervals contain a discrete number of bubbles.

As expected, the high melt viscosity hinders collisions in such a way that the run with H_c is undistinguishable from the one without coalescence. The two other coalescence kernels, on the contrary, visibly affect the size distributions, yielding various levels of overlap between experimental distributions and model outputs. Overall, planar-film coalescence is less efficient than differential-pressure coalescence, and z_1 slightly enhances coalescence efficiency compared to z_2. The match between planar-film coalescence and experimental data is qualitatively the best at higher pressure (or earlier simulation times), whereas the match between differential-pressure coalescence and experimental data is qualitatively better at lower pressure (or later simulation times). Whether coalescence occurred in these experiments by a combination of the two mechanisms, however, needs to be confirmed on the other series of Burgisser and Gardner (2005). It can nonetheless be concluded from this proof of principle that the implementation of kernels H based on different physical mechanisms yields distinct evolutions of the size distributions. Our kinetic model is thus a powerful tool that can help assessing how bubble coalescence occurs in magmas.

4. Discussion

A limitation of our model is that bubble nucleation is ignored. New bubbles could appear under the form of a source term on the right-hand side of Eq. (27), alongside the coalescence kernel terms. Such an extension could be possible without changing the basic form of our kinetic model. Another limitation is that bubble coalescence is assumed to be instantaneous, that is the created bubble is instantly spherical. This approach ignores the time taken by the two merging bubbles to relax into a sphere, which can be significant at high melt viscosity (Navon and Lyakhovsky, 1998; Gardner, 2007; Rust et al., 2003; Castro et al., 2012). If the relaxation time is large, the formation of bubble chain is common (Castro et al., 2012). While the development of bubble chains by successive additions of smaller bubbles can still be considered as binary coalescence, their growth by diffusion and decompression can no longer be approximated by a 1D spherical geometry. Another limiting simplification is the assumption that the volume of the melt shell around the bubbles is constant. Complex interactions are expected between shells as coalescence modifies the shape of the influence zones (i.e. the region where dissolved water is drained into a given bubble). Such heterogeneous spatial distribution of bubbles has been shown to influence nucleation rates (Kedrinskiy, 2009) and growth rates (Gardner et al., 1999). Finally, the addition (initially or by precipitation) of crystals into the melt might influence coalescence, although this effect seems limited when crystals are equant (Okumura et al., 2012).

The planar-film coalescence kernel lacks the scaling symmetry property assumed in the Lovejoy et al. (2004) model. Both the differential-pressure and collision kernels possess this property with a scaling exponent $\beta = 0$ because $H_p(\lambda V, \lambda M, \lambda V', \lambda M') = \lambda^0 H_p(V, M, V', M')$ and $H_c(\lambda V, \lambda V') = \lambda^0 H_c(V, V')$ with $\lambda \in \mathbb{R}$ (deduced from Eqs. (22) and (23), respectively). Focusing on the collision kernel because it is independent
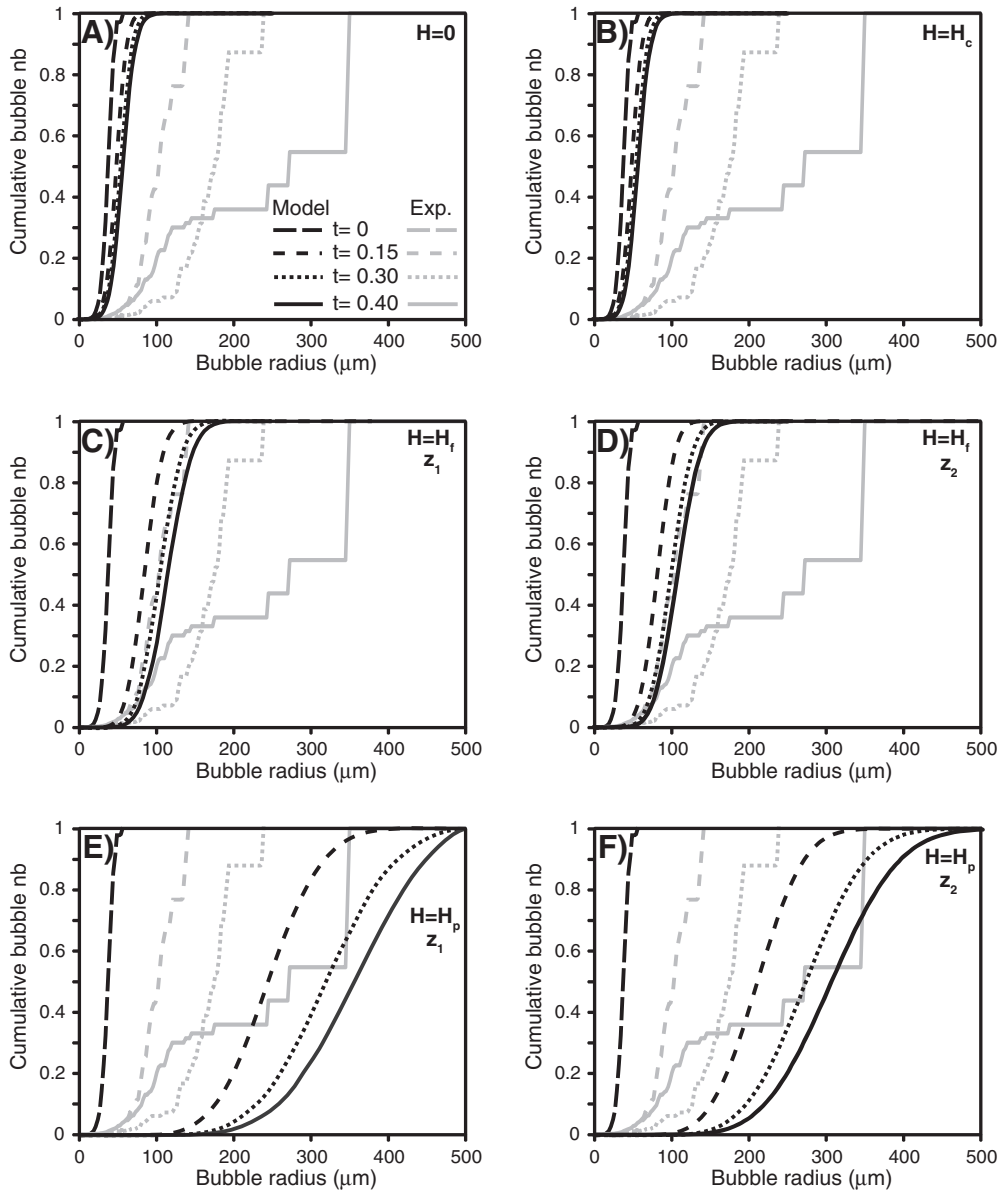
Fig. 5. Comparison between numerical runs and experimental data from Burgisser and Gardner (2005). The initial distributions (long-dashed black curve) correspond to sample PPE4 and to the initial conditions of the runs at $t = 0$ and $\tilde{P}_0 = 40$ MPa. Experimental data quenched at successive times (0.15, 0.3, and 0.4) during the linear decompression (gray curves) are compared with model outputs (black curves). A) Polydisperse bubble growth, no coalescence ($H = 0$). B) Polydisperse bubble growth, collision coalescence ($H = H_c$). C) Polydisperse bubble growth, planar-film coalescence with $z = z_1$ ($H = H_f$). D) Polydisperse bubble growth, planar-film coalescence with $z = z_2$ ($H = H_f$). E) Polydisperse bubble growth, differential-pressure coalescence with $z = z_1$ ($H = H_p$). F) Polydisperse bubble growth, differential-pressure coalescence with $z = z_2$ ($H = H_p$).

of bubble mass, it is straightforward to test whether the long-term evolution of any initial size distribution yields a power law with exponent of β-1 $= -1$ (Lovejoy et al., 2004). We chose an initial size distribution with a constant number of bubbles from 3.3 μm to 692 μm, which reads in the kinetic framework: $f_{0ij}\delta v_i \delta m_j = \mathcal{D}_i \Omega_{ij}/57$ where $\mathcal{D}_i = 1$ and $i = 4...60$. Intervals $\delta \tilde{R}$ started at 2.5 μm and increased of 10% at each successive intervals until $N = 300$ discretization points were created, which yielded a maximum bubble size of 5.95×10^6 m. This large upper bound ensured that all bubbles remained in the simulation domain. Physical values are identical to those of the PPE experimental series (Fig. 4), except the decompression rate, $\Delta \tilde{P} = 0.0025$ MPa s^{-1}, and the viscosity, $\tilde{\eta}_{m0} = 0.1$ Pa s. Both of these low values ensure that the effect of coalescence is maximized during the decompression while calculation time is less than a couple of days.

Fig. 6 shows the evolution of the number density of bubbles with respect to total volume, $\mathcal{N}_v/(\mathcal{W}_0 + \mathcal{V}(t))$, for three different times. The

power-law behavior is visible in all three runs, albeit it is restricted to a small part of the size distribution. As explained in Lovejoy et al. (2004), this is due to the truncated nature of the initial distribution, which causes deviations from the power-law behavior. This example suggests that our model gives results consistent with that of Lovejoy et al. (2004). It also suggests that a slow decompression ($t = 1$ corresponds to 4.4 h) of a low-viscosity magma with initial bubble sizes spanning two orders of magnitude is unlikely to generate clearly defined power-law size distributions by collision coalescence because of truncation effects.

Finally, from a mathematical and numerical modeling point of view, it may be of interest to study the convergence of this kinetic model towards simplified systems of equations. It has been for instance shown that when the relaxation parameters Θ_V and Θ_D converge to zero or infinity, simultaneously or not, several limit situations can be deduced (Barclay et al., 1995; Lyakhovsky et al., 1996; Navon et al., 1998;
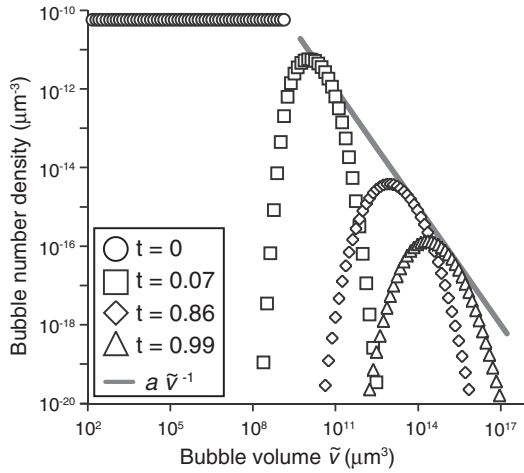
Fig. 6. Evolution of the number density of bubbles as a function of time for a model run with collision coalescence. Three dimensionless simulation times are shown as well as the initial size distribution at $t = 0$ and a power-law distribution (gray line) with an exponent equal to β-1 = −1 and an arbitrary pre-exponential factor (a). Note that it is fortuitous that the balance between growth by decompression/diffusion and by coalescence is such that a single pre-exponential factor seems to fit all three simulation times.

Lensky et al., 2004; Forestier-Coste et al., 2012). Performing an asymptotic analysis on the proposed kinetic model could give simplified equations corresponding to the above limits cases, which would lead to shorter computational times.

5. Conclusions

Starting from the analysis of a monodisperse bubble population done in Lensky et al. (2004) and Forestier-Coste et al. (2012), we propose a simplification of the bubble growth model that removes the coupling between mass evolution and an advection–diffusion equation describing the behavior of the volatile concentration in the melt. We consider instead a mass growth rate converging towards chemical equilibrium for small values of the relaxation parameter Θ_D. If the effective viscosity and water diffusivity are assumed constant during the decompression, monodisperse numerical runs show that this simplification introduces errors of at most 10% on the bubble radius. These differences become negligible when $\Theta_D < 10^{-2}$ or $\Theta_D > 10^{3}$. This simplification as well as the original implementation of the monodisperse model proposed by Forestier-Coste et al. (2012) is included into the open-source software B-Growth that is available as Supplementary data.

In order to simulate both bubble growth and coalescence, we build a kinetic model statistically describing the growth by decompression, exsolution and coalescence of a polydisperse bubble population. The proposed model is homogeneous in space and the distribution function represents the probability to find a bubble of volume v and mass m at time t. The volume and mass growth rates are described by our volatile diffusion simplification of the original monodisperse model. Coalescence is two-dimensional in the kinetic model because its rate involves both the volumes and the masses of the coalescing bubbles. We formulate three coalescence mechanisms based on Castro et al. (2012) and Lovejoy et al. (2004). Numerical simulations based on a semi-implicit numerical scheme show excellent agreement between the coalescence-free runs and the monodisperse runs. When coalescence is introduced, numerical results show that coalescence kernels based on different physical mechanisms yield distinct evolutions of the size distributions. A preliminary comparison between runs and experimental data suggests a qualitative match of two out of the three proposed kernels. This kinetic model is thus a powerful tool that can help assessing how bubble growth and coalescence occur in magmas.

Appendix A. Numerical resolution

The numerical resolution of Eq. (27) consists in a time splitting. At each time step our algorithm first solves explicitly in time the coalescence term (right-hand side of Eq. (27)), and then it solves implicitly in time the expansion term (left-hand side of Eq. (27)). This is equivalent to solve the whole Eq. (27) in a single time step. For $n \in \mathbb{N}$, let us denote the discrete times by t^n, the time steps by $\delta t^n = t^{n+1} - t^n$ and the time discretization of the distribution function by $f^n = f(t^n, v, m)$. The explicit discretization of the coalescence step reads:

$$\hat{f}^{n+1} = f^n + \delta t^n Q(f^n) \tag{A1}$$

where $\hat{f}^{n+1}$ denotes the value of the numerical solution after the coalescence step and has to be used to compute the expansion term. The implicit discretization of the expansion term is given by:

$$f^{n+1} + \delta t^n \left[\frac{\partial}{\partial v} \left(\Gamma^{n+1} f^{n+1} \right) + \frac{\partial}{\partial m} \left(\Psi^{n+1} f^{n+1} \right) \right] = \hat{f}^{n+1}. \tag{A2}$$

Combining the two discretizations, the full, semi-implicit, time discretization of Eq. (27) reads:

$$\frac{f^{n+1} - f^n}{\delta t^n} + \frac{\partial}{\partial v} \left(\Gamma^{n+1} f^{n+1} \right) + \frac{\partial}{\partial m} \left(\Psi^{n+1} f^{n+1} \right) = Q(f^n). \tag{A3}$$

The discretization of the coalescence term has been the subject of Forestier-Coste and Mancini (2012), where a multi-dimensional numerical scheme defined on non-uniform meshes and conserving the first-order moment is described and hence will not be detailed here. In the multi-dimensional framework, one must choose which first moment to conserve because it is numerically impossible to conserve simultaneously all the first moments. Since the coalescence process conserves mass, we choose to conserve the moment representing the total mass of water $\mathcal{M}(t) = \Lambda_{0,1}(t)$. This model is among the few considering two-dimensional coalescence; numerical schemes for this kind of problem have not yet been widely studied (Qamar and Warnecke, 2007a, 2007b; Qamar et al., 2009).

The scheme solving the expansion term is implicit in time because we want to avoid a stability condition (CFL) for this time discretization. Solving explicitly the expansion term would imply a CFL condition on the time step δt^n, which is bounded by the minimum of the relaxation parameters Θ_V and Θ_D. This causes very long computational times, in particular when considering the chemical and/or mechanical equilibrium ($\Theta_V \ll 1$ and/or $\Theta_D \ll 1$). By using instead an implicit scheme, the time step is fixed by the positivity condition on the coalescence term, which is only bounded by Θ_V (Forestier-Coste and Mancini, 2012).

The experimental measurements are usually defined by bubble radii on a uniform mesh, which conditions the discretization in v and m. This distribution of initial radii is chosen as the basis to write the grid mesh in volume and mass while assuming that measurements are done at the thermodynamical equilibrium. Hence, fixing N grid points, we have for $i = 1 \ldots N$ the following definitions for the mesh points in v and m:

$$v_{i-1/2} = \left(\frac{\tilde{R}_{min} + i\delta\tilde{R}}{\tilde{R}_0} \right)^3, \, m_{i-1/2} = v_{i-1/2} + \sum v_{i-1/2}^{2/3} \tag{A4}$$

where $\tilde{R}_0$ is the mean dimensional radius of the initial data (used also for the scaling), $\tilde{R}_{min}$ is the minimum dimensional radius considered in the simulation, and $\delta\tilde{R}$ is the dimensional step of the uniform grid defining the initial data. The space mesh sizes are then defined as $\delta v_i = v_{i+1/2} - v_{i-1/2}$ and $\delta m_i = m_{i+1/2} - m_{i-1/2}$. Middle grid points are defined as $v_i = (v_{i+1/2} + v_{i-1/2})/2$ and $m_i = (m_{i+1/2} + m_{i-1/2})/2$.

For $n \in \mathbb{N}$ and $i,j = 1...N$, we can now define the discrete distribution function f^n_{ij}, which is an approximation of $f(t^n,v_i,m_j)$, and the discrete marginal distribution with respect to volume, $\mathcal{N}^n_v$:

$$\mathcal{N}^n_v(v_i) = \sum_{j=1}^{N} f^n_{ij}\delta m_j \tag{A5}$$

The numerical resolution of the expansion part is split in two: first the discretization implicit in time of the term $\frac{\partial}{\partial v}(\Gamma f)$ then that of $\frac{\partial}{\partial m}(\Psi f)$. This is equivalent to a directional splitting, solving first:

$$\frac{\partial f}{\partial t} + \frac{\partial}{\partial v}(\Gamma f) = 0 \tag{A6}$$

and then:

$$\frac{\partial f}{\partial t} + \frac{\partial}{\partial m}(\Psi f) = 0. \tag{A7}$$

Since the resolution of both equations is similar, we only report the implicit, finite difference scheme for Eq. (A6). Let j be fixed, $i = 1...N$, and define:

$$\Gamma^n_{ij} = \frac{3}{\eta\Theta_V}\left(m_j - v_i(1-t) - \Sigma v_i^{2/3}\right) \tag{A8}$$

and its positive and negative parts: $(\Gamma^+)^n_{ij} = \max(0,\Gamma^n_{ij})$, $(\Gamma^-)^n_{ij} = \min(0,-\Gamma^n_{ij})$. Eq. (A6) is then discretized implicitly in time by:

$$\left(1 + \frac{\delta t}{\delta v_i}\left|v^{n+1}_{ij}\right|\right)f^{n+1}_{ij} - \frac{\delta t}{\delta v_i}\left[(\Gamma^+ f)^{n+1}_{i-1,j} + (\Gamma^- f)^{n+1}_{i+1,j}\right] = f^n_{ij}. \tag{A9}$$

To solve this implicit bi-dimensional scheme we transform it by writing the unknown square matrix f^n_{ij} of size $N \times N$, in a vector X^n_h of size N^2. For each time step n and index $j = 1...N$, we define $h = i + (j-1)N$ for $i = 1...N$ and $X^n_h = f^n_{ij}$, that is:

$$X^n = \left(f^n_{1,1}, f^n_{2,1}, f^n_{3,1}, ..., f^n_{N-2,N}, f^n_{N-1,N}, f^n_{N,N}\right)^T \tag{A10}$$

Vectors a^n and c^n of size $N^2 - 1$ are defined for $j = 1...N$ by:

$$a^n_h = \begin{cases} -\frac{\delta t}{\delta v_i}(\Gamma^-)^n_{i+1,j}, & i = 1...N-1 \\ 0, & i = N \end{cases} \tag{A11}$$

$$c^n_h = \begin{cases} -\frac{\delta t}{\delta v_i}(\Gamma^+)^n_{i-1,j}, & i = 2...N \\ 0, & i = 1 \end{cases} \tag{A12}$$

The vector b^n of size N^2 for $i,j = 1...N$ is:

$$b^n_h = 1 + \frac{\delta t}{\delta v_i}\left|\Gamma^n_{ij}\right| \tag{A13}$$

and the hth line of the tridiagonal matrix $\mathcal{B}^n$ reads $\mathcal{B}^n_h = (0...0 \ c^n_h b^n_h a^n_h \ 0...0)$. The discrete Eq. (A9) then reads:

$$\mathcal{B}^{n+1}_{h,h-1}X^{n+1}_{h-1} + \mathcal{B}^{n+1}_{h,h}X^{n+1}_h + \mathcal{B}^{n+1}_{h,h+1}X^{n+1}_{h+1} = X^n_h \tag{A14}$$

which is solved by a LU decomposition. At each time step n the whole algorithm for the expansion term involves the successive resolution of

Eqs. (A6) and (A7) before returning to the resolution of the coalescence part.

Appendix B. Alternate inter-bubble distance formulation

A formulation of the inter-bubble distance, z_1, taking into account melt shell overlap can be found using the geometry depicted in Fig. B1. If e is the thickest part of the lens created by the overlap of the melt shells (light gray region in Fig. B1) and d is the distance between the two bubble centers, it follows that $z_1 = S + S' - R - R' - e = d - R - R'$. The volume of the lens is given by $\pi e^2[d^2 + 2d(S + S') - 3(S - S')^2]/(12d)$. One way that all the melt shells approximately fill the entire space available is to enforce that the volume of the lens equals that of the small volume wedged between the melt shells (plateau border, dark gray region in Fig. B1). This is an approximation as the full volume distribution, and not just a bubble pair, controls how well the space is filled. We note, however, that even with full distribution known, finding an optimal spatial arrangement is challenging (e.g., Baranau and Tallarek, 2014). Here we restrict the reasoning to bubble pairs, and we ensure that the bubble network fulfills the criterion of maximum packing (see below). We further assume that the volume wedged between the melt shells is equal to ke^3, where k is a proportionality constant to be determined.

The inter-bubble distance can be calculated by equating lens and wedge volumes, which leads to a second order equation on z_1:

$$z_1 = \frac{-u_2 + \sqrt{u_2^2 - 4u_1u_3}}{2u_1}$$

$$u_1 = \frac{1 + 12k/\pi}{R(1+o)}$$

$$u_2 = 2 + 2\alpha^{-1/3} + 12k\left(2 - \alpha^{-1/3}\right)/\pi$$

$$u_3 = R(1+o)$$
$$\times \left[1 - 3\alpha^{-2/3}\left(\frac{1-o}{1+o}\right)^2 + 2\alpha^{-1/3} + 12k\left(1 - \alpha^{-1/3}\right)/\pi\right] \tag{B1}$$

where $o = R'/R$. The value of k can be set for the whole distribution by defining the conditions of maximum packing. It occurs at a critical volume fraction α_p and implies that $z_1 = 0$. Setting these conditions in Eq. (B1) yields a relationship between k, α_p, and o:

$$k = \frac{\pi}{12\left(\alpha_p^{-1/3} - 1\right)}\left[1 + 2\alpha_p^{-1/3} - 3\alpha_p^{-2/3}\left(\frac{1-o}{1+o}\right)^2\right]. \tag{B2}$$
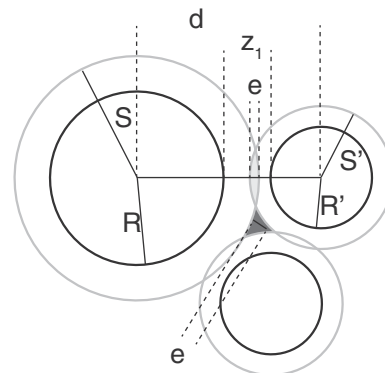

Fig. B1. Detail of the geometrical configuration of a bubble pair in Fig. 1.
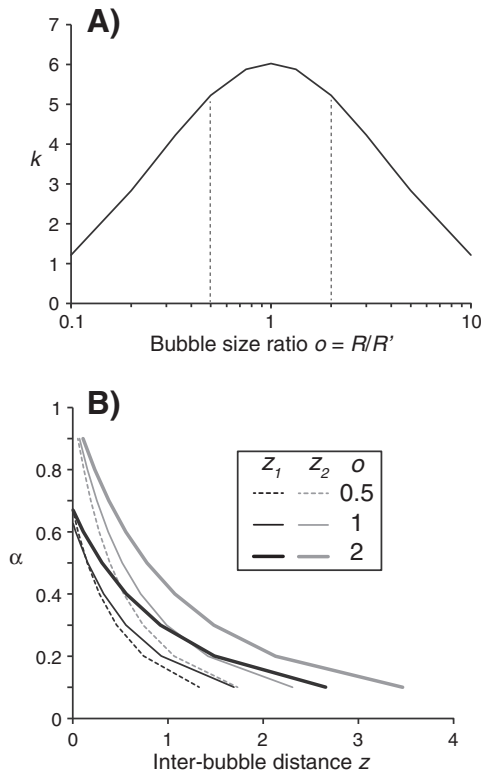
Fig. B2. A) Proportionality factor k as a function of bubble size ratio. Vertical dashed lines frame the common span of ratio observed in experiments. B) Inter-bubble distance (z) as a function of porosity (α) for two calculation methods (z_1 and z_2). Curves for three bubble size ratios (o) are shown.

There is no general law to find α_p in polydisperse distributions, the value of which starts at the random packing for monodisperse spheres, ~0.63, and increases with the spread of the size distribution (Farr and Groot, 2009; Baranau and Tallarek, 2014). The bubble size distributions in the experiments of Burgisser and Gardner (2005) mostly remain within a factor 2 of the median bubble size. Following Farr and Groot (2009), this constraint yields $\alpha_p \approx 0.67$. The ratio o, which is not known a priori, strongly controls k (Fig. B2A). The same constraint, $0.5 < o < 2$, however, suggests that it is possible to use one representative value, $k \approx 5$, for the whole distribution. Fig. B2B shows a simple comparison between z_1 and z_2 for bubble radius $\bar{R}_0 = 10\ \mu m$, $k = 5$, and o varying from 0.5 to 2. As expected, z_1 yields distances that vanish around α_p. They are shorter than z_2 at high porosity and low values of o but higher otherwise; using z_1 thus tends to slow down coalescence compared to z_2 at high α and for bubbles of similar sizes.

Appendix C. Supplementary data

Supplementary data to this article can be found online at http://dx.doi.org/10.1016/j.jvolgeores.2016.01.016.

References

Bai, L., Baker, D., Hill, R.J., 2010. Permeability of vesicular Stromboli basaltic glass: lattice Boltzmann simulations and laboratory measurements. J. Geophys. Res. 115, B07201. http://dx.doi.org/10.1029/2009JB007047.

Baranau, V., Tallarek, U., 2014. Random-close packing limits for monodisperse and polydisperse hard spheres. Soft Matter 10, 3826–3841.

Barclay, J., Riley, D.S., Sparks, R.S.J., 1995. Analytical models for bubbles growth during decompression of high viscosity magmas. Bull. Volcanol. 57, 422–431.

Berry, E.X., 1967. Cloud droplet growth by collection. J. Atmos. Sci. 24, 688–701.

Blower, J.D., 2001. Factors controlling permeability–porosity relationships in magma. Bull. Volcanol. 63, 497–504.

Blower, J.D., Keating, J.P., Mader, H.M., Phillips, J.C., 2001. Inferring volcanic degassing processes from vesicle size distributions. Geophys. Res. Lett. 28, 347–350.

Burgisser, A., Degruyter, W., 2015. Magma ascent and degassing at shallow levels. In: Sigurdsson (Ed.), Encyclopedia of Volcanoes, second ed. Academic Press, San Diego, pp. 225–236.

Burgisser, A., Gardner, J., 2005. Experimental constraints on degassing and permeability in volcanic conduit flow. Bull. Volcanol. 67, 42–56.

Carrillo, J.A., Desvillettes, L., Fellner, K., 2008. Exponential decay towards equilibrium for the inhomogeneous Aizenman–Bak model. Commun. Math. Phys. 278 (2), 433–451.

Castro, J.M., Burgisser, A., Schipper, I., Mancini, S., 2012. Mechanisms and dynamics of bubble coalescence in silicic magmas. Bull. Volcanol. 74 (10), 2339–2352.

Chernov, A.A., Kedrinsky, V.K., Pil'nik, A.A., 2014. Kinetics of gas bubble nucleation and growth in magmatic melt at its rapid decompression. Phys. Fluids 26, 116602. http://dx.doi.org/10.1063/1.4900846.

Chouet, B., Dawson, P., Nakano, M., 2006. Dynamics of diffusive bubble growth and pressure recovery in a bubbly rhyolitic melt embedded in an elastic solid. J. Geophys. Res. 111, B07310. http://dx.doi.org/10.1029/2005JB004174.

Degruyter, W., Bachmann, O., Burgisser, A., Manga, M., 2012. The effects of outgassing on the transition between effusive and explosive silicic eruptions. Earth Planet. Sci. Lett. 349-350, 161–170.

Doube, M., Kłosowski, M.M., Arganda-Carreras, I., Cordeliéres, F., Dougherty, R.P., Jackson, J., Schmid, B., Hutchinson, J.R., Shefelbine, S.J., 2010. BoneJ: free and extensible bone image analysis in ImageJ. Bone 47, 1076–1079. http://dx.doi.org/10.1016/j.bone.2010.08.023.

Eichelberger, J.C., Carrigan, C.R., Westrich, H.R., Price, R.H., 1986. Non-explosive silicic volcanism. Nature 323, 598–602.

Escobedo, M., Laurençot, P., Mischler, S., 2004. On a kinetic equation for coalescing particles. Commun. Math. Phys. 246 (2), 237–267.

Farr, R.S., Groot, R.D., 2009. Close packing density of polydisperse hard spheres. J. Chem. Phys. 131, 244101. http://dx.doi.org/10.1063/1.3276799.

Filbet, F., Laurençot, P., 2004. Numerical simulation of the Smoluchowski equation. SIAM J. Sci. Comput. 25, 2004–2028.

Forestier-Coste, L., Mancini, S., 2012. A finite volume preserving scheme on nonuniform meshes and for multidimensional coalescence. SIAM J. Sci. Comput. 34 (6), B840–B860.

Forestier-Coste, L., Mancini, S., Burgisser, A., James, F., 2012. Numerical resolution of a monodisperse model of bubble growth in magmas. Appl. Math. Model. 36, 5936–5951.

Gaonac'h, H., Lovejoy, S., Stix, S., Scherzter, D., 1996. A scaling growth model for bubbles in basaltic lava flows. Earth Planet. Sci. Lett. 139, 395–409.

Gaonac'h, H., Lovejoy, S., Schertzer, D., 2003. Percolating magmas and explosive volcanism. Geophys. Res. Lett. 30. http://dx.doi.org/10.1029/2002GL016022.

Gaonac'h, H., Lovejoy, S., Carrier-Nunes, M., Schertzer, D., Lepine, F., 2007. Percolating magmas in three dimensions. Nonlinear Process. Geophys. 14, 743–755.

Gardner, J.E., 2007. Bubble coalescence in rhyolitic melts during decompression from high pressure. J. Volcanol. Geotherm. Res. 166, 161–176.

Gardner, J.E., 2009. The impact of pre-existing gas on the ascent of explosively erupted magma. Bull. Volcanol. 71, 835–844.

Gardner, J.E., Hilton, M., Carroll, M.R., 1999. Experimental constraints on degassing of magma: isothermal bubble growth during continuous decompression from high pressure. Earth Planet. Sci. Lett. 168, 201–218.

Hess, K.-U., Dingwell, D.B., 1996. Viscosities of hydrous leucogranitic melts: a non-Arrhenian model. Am. Mineral. 81, 1297–1300.

Iacono Marziano, G., Schmidt, B.C., Dolfi, D., 2007. Equilibrium and disequilibrium degassing of a phonolitic melt (Vesuvius AD 79 "white pumice") simulated by decompression experiments. J. Volcanol. Geotherm. Res. 161, 151–164.

Ichihara, M., 2008. Dynamics of a spherical viscoelastic shell: implications to a criterion for fragmentation/expansion of bubbly magma. Earth Planet. Sci. Lett. 265, 18–32.

Jaupart, C., Allègre, C., 1991. Gas content, eruption rate and instabilities of eruption regime in silicic volcanoes. Earth Planet. Sci. Lett. 102, 413–429.

Kedrinskiy, V., 2009. Hydrodynamic aspects of explosive eruptions of volcanoes: simulation problems. Shock Waves 18, 451–464.

Kumar, R., Kumar, J., Warnecke, G., 2011. Numerical methods for solving two-dimensional aggregation population balance equations. Chem. Eng. Sci. 35, 999–1009.

Larsen, J.F., Gardner, J.E., 2000. Experimental constraints on bubble interactions in rhyolite melts: implications for vesicle size distribution. Earth Planet. Sci. Lett. 180, 201–214.

Larsen, J.F., Denis, M.-H., Gardner, J.E., 2004. Experimental study of bubble coalescence in rhyolitic and phonolitic melts. Geochim. Cosmochim. Acta 68, 333–344.

Lensky, N.G., Lyakhovsky, V., Navon, O., 2001. Radial variations of melt viscosity around growing bubbles and gas overpressure in vesiculating magmas. Earth Planet. Sci. Lett. 186, 1–6.

Lensky, N.G., Navon, O., Lyakhovsky, V., 2004. Bubble growth during decompression of magma: experimental and theoretical investigation. J. Volcanol. Geotherm. Res. 129, 7–22.

L'Heureux, I., 2007. A new model of volatile bubble growth in a magmatic system: isobaric case. J. Geophys. Res. 112, B12208. http://dx.doi.org/10.1029/2006JB004872.

Lovejoy, S., Gaonac'h, H., Schertzer, D., 2004. Bubble distributions and dynamics: the expansion–coalescence equation. J. Geophys. Res. 109, B11. http://dx.doi.org/10.1029/2003JB002823.

Lyakhovsky, V., Hurwitz, S., Navon, O., 1996. Bubble growth in rhyolitic melts: experimental and numerical investigation. Bull. Volcanol. 58, 19–32.

Martel, C., Iacono-Marziano, G., 2015. Timescales of bubble coalescence, outgassing, and foam collapse in decompressed rhyolitic melts. Earth Planet. Sci. Lett. 412, 173–185.

Navon, O., Lyakhovsky, V., 1998. Vesiculation processes in silicic magmas. In: Gilbert, J.S., Sparks, R.S.J. (Eds.), The Physics of Explosive Volcanic Eruptions 145. Geol. Soc. Spec. Pub., London, pp. 27–50.

Navon, O., Chekhmir, A., Lyakhovsky, V., 1998. Bubble growth in highly viscous melts: theory, experiments, and autoexplosivity of dome lavas. Earth Planet. Sci. Lett. 160, 763–776.

Ni, H., Zhang, Y., 2008. H$_2$O diffusion models in rhyolitic melt with new high pressure data. Chem. Geol. 250, 68–78.

Nishimura, T., 2004. Pressure recovery in magma due to bubble growth. Geophys. Res. Lett. 31, L12613. http://dx.doi.org/10.1029/2004GL019810.

Okumura, S., Nakamura, M., Nakano, T., Uesugi, K., Tsuchiyama, A., 2012. Experimental constraints on permeable gas transport in crystalline silicic magmas. Contrib. Mineral. Petrol. 164, 493–501.

Proussevitch, A.A., Sahagian, D.L., 1998. Dynamics and energetics of bubble growth in magmas: analytical formulation and numerical modeling. J. Geophys. Res. 103, 18223–18251.

Proussevitch, A.A., Sahagian, D.L., Anderson, A.T., 1993a. Dynamics of diffusive bubble growth in magmas: isothermal case. J. Geophys. Res. 98, 22283–22307.

Proussevitch, A.A., Sahagian, D.L., Kutolin, V.A., 1993b. Stability of foams in silicate melts. J. Volcanol. Geotherm. Res. 59, 161–178.

Qamar, S., Warnecke, G., 2007a. Solving population balance equations for two-component aggregation by a finite-volume scheme. Chem. Eng. Sci. 62, 679–693.

Qamar, S., Warnecke, G., 2007b. Numerical solution of population balance equations for nucleation growth and aggregation processes. Comput. Chem. Eng. 31, 1576–1589.

Qamar, S., Warnecke, G., Elsner, M., 2009. On the solution of population balances for nucleation, growth, aggregation and breakage processes. Chem. Eng. Sci. 64, 2088–2095.

Rust, A.C., Cashman, K.V., 2011. Permeability controls on expansion and size distributions of pyroclasts. J. Geophys. Res. 116, B11202. http://dx.doi.org/10.1029/2011JB008494.

Rust, A.C., Manga, M., Cashman, K.V., 2003. Determining flow type, shear rate and shear stress in magmas from bubble shapes and orientations. J. Volcanol. Geotherm. Res. 122 (1–2), 111–132.

Saar, M.O., Manga, M., 1999. Permeability–porosity relationship in vesicular basalts. Geophys. Res. Lett. 26, 111–114.

Sparks, R.S.J., 1978. The dynamics of bubble formation and growth in magmas: a review and analysis. J. Volcanol. Geotherm. Res. 3, 1–37.

Takeuchi, S., Nakashima, S., Tomiya, A., Shinohara, H., 2005. Experimental constraints on the low gas permeability of vesicular magma during decompression. Geophys. Res. Lett. 32, L10312. http://dx.doi.org/10.1029/2005GL022491.

Toramaru, A., 1989. Vesiculation process and bubble size distributions in ascending magmas with constant velocities. J. Geophys. Res. 94, 17523–17542.

Toramaru, A., 1995. Numerical study of nucleation and growth of bubbles in viscous magmas. J. Geophys. Res. 100, 1913–1931.

Woods, A.W., Koyaguchi, T., 1994. Transitions between explosive and effusive eruptions of silicic magmas. Nature 370, 641–644.